



NTNU – Trondheim
Norwegian University of
Science and Technology

Development of car for Eco-marathon

Aksel Qviller

Master of Science in Engineering and ICT

Submission date: March 2012

Supervisor: Knut Einar Aasland, IPM

Norwegian University of Science and Technology

Department of Engineering Design and Materials

NORGES TEKNISK-
NATURVITENSKAPELIGE UNIVERSITET
INSTITUTT FOR PRODUKTUTVIKLING
OG MATERIALER

MASTEROPPGAVE HØST 2011 FOR STUD.TECHN. AKSEL QVILLER

UTVIKLING AV ECO-MARATHON-BIL Development of car for Eco-marathon

Shell Eco-Marathon er en konkurranse mellom studentgrupper om å utvikle, bygge og kjøre den mest energigjerrige bilen. Konkurransen går årlig i Europa i mai, og den har nå gått i over 25 år. Siste år var det drøyt 200 deltakende lag. NTNU har vært med de fire siste årene, og har oppnådd to andre- og en førsteplass i klassen "urban concept", med henholdsvis 729km/l, 99km/kWh og 1246 km/l. Det siste er rekord for klassen gjennom alle tider.

For våren 2012 vil vi gjøre mye nyutvikling. Vi har høstet mye erfaring med karosseriet og bilkonseptet vårt, og det kan være aktuelt å utvikle en ny bil. Det er også endringer i rammebetingelsene: Løpet vil nå gå i bygater, noe som stiller nye krav til hjuloppheng. Det skal etableres en ny prosjektgruppe med ansvar for å utvikle og lage bilen for 2012. Prosjektet er et samarbeidsprosjekt mellom et antall studenter fra flere ulike fagmiljø ved NTNU, og det forutsetter også sponsorarbeid, arbeidet med de dokumentene som er nødvendige for å melde på bilen til konkurransen samt organisering og gjennomføring av selve løpet våren 2012. Dvs. prosjektoppgaven videreføres i masteroppgaven.

Om utgangspunktet skal være 2011-bilen eller om det skal begynnes med et nytt karosseri, vil være en beslutning for prosjektgruppen og veilederne sammen. Uansett er det mye som må utvikles. Vi har hittil basert oss på en brenselcelle-løsning med en stack fra Ballard, men dette må vi muligens gå bort fra, da Ballard har inngått en avtale med Daimler AG som forbyr bruk av Ballard-teknologi i biler uten tilknytning til Mercedes. Det er derfor et stort antall problemområder som må utforskes og der det må tas viktige beslutninger:

- brenselcelle
- elektromotor
- muligheter for energilagring mellom celle og motor
- hjuloppheng – muligheter for fjæring
- styring og innstilling av forhjulsgeometri
- betjening og ergonomi – betjening og kommunikasjon mot fører
- karosseri – nytt eller videreutviklet

Det spesifikke området for denne kandidaten må avtales med de andre i prosjektgruppa. Det skal framgå tydelig av rapporten hvilke(n) del(er) eller område(r) kandidaten har hatt ansvar for.

Vi legger stor vekt på god prosjektstyring.

Det er ikke mulig å jobbe med dette prosjektet uavhengig av de andre: Det er helheten – den resulterende bilen og gjennomføringen av gruppeprosjektet som teller.

I tillegg til prosjektrapporten, skal det leveres en PU-journal i instituttets A3-format.

Oppgaven skal inneholde:

- en gjennomgang av bilen for å fastslå dagens status i forhold til de nye kravene som har kommet
- identifisering av område som denne kandidaten skal jobbe med
- idegenerering og konseptutvikling på utvalgt(e) område(r)
- i størst mulig grad utvikling av aktuelle deler
- dokumentasjon av resultatene

I tillegg til dette skal kandidaten yte sitt bidrag inn i prosjektgruppa på alle de ikke-tekniske områdene som også må løses.

Rapporten skal holdes kort. Som vedlegg ønsker vi prosjektrapporten som fra de andre gruppemedlemmene, slik at helheten framgår. Det kan refereres til prosjektrapporten der det er relevant.

Før kandidaten går i gang med arbeidet, skal han/hun sette opp en oversiktlig plan som inneholder alle opplysninger om metodikk og betingelser. Planen skal foreligge til godkjenning innen tre uker etter utlevering av oppgaven.

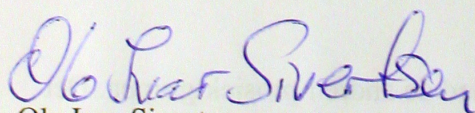
Besvarelsen redigeres mest mulig som en forskningsrapport med et sammendrag på norsk og engelsk, konklusjon, litteraturliste, innholdsfortegnelse, etc. Ved utarbeidelse av teksten skal kandidaten legge vekt på å gjøre teksten oversiktlig og velskrevet. Med henblikk på lesning av besvarelsen er det viktig at de nødvendige henvisninger for korresponderende steder i tekst, tabeller og figurer anføres på begge steder.

Senest 3 uker etter oppgavestart skal et A3 ark som illustrerer arbeidet leveres inn. En mal for dette arket finnes på instituttets hjemmeside under menyen undervisning. Arket skal også oppdateres ved innlevering av masteroppgaven.

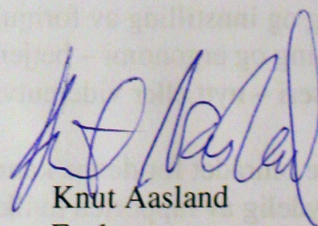
Besvarelsen skal leveres i papirformat i to eksemplarer. Lever også en elektronisk versjon av oppgaven på CD eller DVD i pdf-format.

Kontaktperson hos Shell: Kim Bye Brun

Kontaktperson hos DNV: Kristina Dahlberg



Ole Ivar Sivertsen
Instituttleder



Knut Aasland
Faglærer



NTNU
Norges teknisk-
naturvitenskapelige universitet

Institutt for produktutvikling
og materialer

Abstract

The objective of this project has been to develop the front suspension and certain parts of the in-wheel motor of NTNU's new car for Shell Eco-marathon, as well as assisting other team members.

NTNU has participated in the Urban Concept class in the European race every year since 2008, with one world record (2009), twice second place, and one failure (2010). The original *PureChoice* car (renamed *DNV Fuel Fighter* during the second year) was powered by hydrogen, but the power source was changed to battery this year as a team decision to avoid the pitfalls and challenges with working with a hydrogen fuel cell.

Shell Eco-marathon 2012 moves the competition from the typical, smooth, race track to the city streets of Rotterdam. This requires a complete redesign of the suspension to handle the new type of road, since the previous designs have been completely rigid. By not only upgrading the suspension, but also building a completely new car body, new and better mounting points for the suspension could be made and realize fully damped suspension on all four wheels. The new motor specification also allowed the in-wheel motor to be made both lighter and more compact.

This work is part of the collective work of more than ten engineering students at NTNU where I have been working towards an earlier delivery of a thesis than the rest of the team because of starting my thesis during the fall. My main responsibilities were in the beginning only the front suspension, with some shared responsibility of the rear suspension. After sketching and presenting a CAD model of how the new motor wheel could be constructed I also became much more involved with the design of the motor wheel which will be lighter and more compact than the previous in-wheel motors.

This report is divided into three sections – the first discusses the front suspension, the second discusses the mechanical motor design, and the third is a collection of appendices with technical data. All illustrations are self-made unless stated otherwise.

Sammendrag

Målet med dette prosjektet har vært å utvikle det nye forhjulsopphenget og enkelte deler i den nye motoren til NTNUs nye bil for Shell Eco-marathon.

NTNU har deltatt i Urban Concept-klassen i den europeiske konkurransen hvert år siden 2008, med én verdensrekord (2009), to ganger på annenplass, og ett nederlag (2010). Den tidligere *PureChoice*-bilen (døpt om til *DNV Fuel Fighter* i annet år) var drevet av hydrogen, men energikilden har nå i år blitt endret til batteri for å unngå utfordringene og problemene tilknyttet arbeidet med brenselcellen.

Shell Eco-marathon 2012 flytter konkurransen fra racingbane til bygater i Rotterdam. Dette gjør at hjulopphenget må redesignes for å hankses med det nye underlaget, siden det tidligere har vært fullstendig stivt. Ved å ikke bare oppgradere hjulopphenget, men å bygge en helt ny bil, med nye og bedre festepunkter til hjuloppheng kunne et fulldempet hjuloppheng realiseres. Den nye motorspesifikasjonen tillater også at motoren, som bygges inn i det ene bakhjulet, blir både lettere og mer kompakt.

Dette arbeidet er del av et kollektivt verk med mer enn ti ingeniørstudenter, hvor jeg har jobbet mot en tidligere innleveringsfrist enn de andre på teamet grunnet masteruttak på høsten. Mine ansvarsområder var i utgangspunktet bare forhjulsopphenget, med noe delt ansvar for bakhjulsoppheng. Etter å ha skissert og presentert en mulig løsning for hvordan den nye motoren kunne bygges ble dette også en stor del av mine ansvarsområder.

Denne rapporten er delt inn i tre deler – den første delen omhandler forhjulsopphenget, mens den andre delen handler om motorhjulet, og den tredje delen er en samling tekniske vedlegg. Alle illustrasjoner er selvlagd med mindre annet er indikert.

Preface

This master thesis documents my efforts to design and produce the front suspension of NTNU's new Shell Eco-marathon car, *DNV Fuel Fighter 2*.

This is the second time I get to work on the Shell Eco-marathon project at NTNU. The first time was during my specialization project during the spring of 2011, and as such I am privileged to have the opportunity to bring the experience and knowledge gained (from working on the original *DNV Fuel Fighter*) into the construction of a completely new vehicle.

As a team project with more than ten team members, the progression has adhered to a common plan for design, manufacturing, assembly and testing, while my thesis' period only overlaps with the start of the project. At the time of writing and delivery of this thesis, many parts are still in production. As a result, there was very little time to write this report; I did not have the time to cover everything or as well as I wanted to. The production, delayed by factors such as late delivery of materials and design finalization, has needed a lot of attention since this project has such high stakes with regards to prestige and economy.

The report discusses work that has been done in close co-operation with and by others on the team. The rest of the team delivered their specialization project report in December 2011. As part of this report, I wrote a chapter on the front suspension, hubs and axles, as an aid to fill in what would else be missing pieces. This thesis makes references to and draws on the work done in that report, and where there should be any major differences, this text prevails.

I would like to thank my supervisor, fellow team members – of both the 2011 and 2012 teams – for allowing me to work on this intriguing and challenging project. The practical aspects have enabled a much deeper sense of commitment and motivation. Also, thanks to the main sponsors and production partners for engaging in and allowing the project to proceed with considerable funding. I hope my work will pay off on the race track in Rotterdam and that the supervisors and sponsors will be pleased with the end results.

Aksel Qviller, Trondheim 2012

Table of contents

Abstract.....	3
Sammendrag	4
Preface	5
Table of contents	7
Tables	9
Figures	10
1. Introduction	13
1.1. The team.....	14
1.2. Sponsors	16
2. Front suspension.....	17
2.1. Requirements.....	17
2.2. Concept selection.....	19
2.3. Geometry optimization and force determination.....	20
2.3.1. Camber change.....	21
2.3.2. Wishbone angles	22
2.3.3. Calculation of link forces	23
2.3.4. Calculation of coilover forces.....	28
2.3.5. Calculation of tie-rod forces	28
2.3.6. Anti-dive.....	29
2.4. Hubs	30
2.5. Axles	32
2.6. Steering knuckles.....	33
2.6.1. Ackerman steering	34
2.6.2. Strength.....	36
2.6.3. Production of steering knuckles.....	38
2.6.4. Milling of carbon fiber	39
2.7. Linkages	40
2.7.1. Link strength.....	40
2.7.2. Wishbone connectors	42
2.7.3. Tie rods.....	45
2.7.4. Roll- and strut bar.....	45
2.8. Mounting points.....	45
3. Motor design	49
3.1. Requirements.....	49
3.2. Concept description	50
3.3. Hub and axle.....	51
3.4. Rotors	54
3.5. Rim adapters.....	57
3.6. Test rig and SmartMotor-adapter.....	58
4. Conclusions	61
5. References	63
6. Appendices.....	65
6.1. Appendix 1: Acknowledgments	66
6.2. Appendix 2: Estimated material data for DB 420 [+45/-45].....	67
6.3. Appendix 3: Program listings	68

6.4.	Appendix 4: Spreadsheet for simplified vehicle dynamics.....	71
6.5.	Appendix 5: Race track map	72

Tables

Table 1: Front suspension requirement specification.....	17
Table 2: Trade-off matrix for front suspension concepts	19
Table 3: Dimensioning forces acting on wheels [from Gudvangen et al 2011]	23
Table 4: Trade-off matrix for steering knuckle material selection	34
Table 5: Table of minimum pitch and minor diameters of ISO M6 and M8.....	40
Table 6: Requirements specification for mechanical motor parts.....	49
Table 7: DB 420 physical properties	67

Figures

Figure 1: The final front suspension	17
Figure 2: Double wishbone concept, parts annotated	20
Figure 3: Typical steering knuckle concept	20
Figure 4: Camber angle change during spring action	22
Figure 5: Top view of front left suspension links	22
Figure 6: Viewed from beneath, front right suspensions	23
Figure 7: Rear view of front left suspension links	23
Figure 8: Forces acting on wheels [1]	23
Figure 9: Rigid body model of front suspension, where P_B and P_C are the braking and cornering forces, and $C_{1,2,3,4}$ are the support forces acting through the wishbone links	24
Figure 10: Force and constraints on the knuckle	24
Figure 11: Simplified force and torque on knuckle	24
Figure 12: Steering knuckle modeled as a beam with load and reaction forces	25
Figure 13: Constraint model for top arms during braking	26
Figure 14: Constraint model for lower arms during braking	26
Figure 15: Constraint model for top arms during cornering	27
Figure 16: Constraint model for lower arms during cornering	27
Figure 17: Diagram of weight force and link geometry view from behind the car, where P_W is the weight on the wheel and C_5 is the coilover's reaction force	28
Figure 18: Sketch setup in NX to obtain measurements for anti-dive calculations	29
Figure 19: Force diagram of dive/anti-dive contributing forces	29
Figure 20: Front and back view of the hub	30
Figure 21: View of hub assembly	30
Figure 22: FEM analysis of hub during braking	31
Figure 23: FEM analysis of hub during cornering	31
Figure 24: Hubs and coilover parts received from Nomek	32
Figure 25: CAD model of axle	32
Figure 26: FEM analysis of axle during braking	33
Figure 27: Ackerman steering based on sketch in the PD-journal, wheels and angles annotated. α is the typical toe-angle when driving straight ahead.	34
Figure 28: 3D view of steering radius check	35
Figure 29: Verification of ackerman steering for 20 m turning radius	36
Figure 30: Verification of 6 m turning radius requirement	36
Figure 31: Finding the smallest possible turning radius, tilted view.	36
Figure 32: FEM analysis of knuckle during braking	37
Figure 33: FEM analysis of knuckle during cornering	37
Figure 34: Unidirectional carbon fiber wrapping for reinforcement of bolted connections	38
Figure 35: Mold for carbon fiber knuckles	39
Figure 36: Link consisting of rod ends and nuts	40
Figure 37: Single rod end on bottom, double rod ends on top	42
Figure 38: Solid lower wishbone	42
Figure 39: Connector and link rods	42
Figure 40: 3D views of the left wishbone connector	43

Figure 41: Left suspension with connector and coilover.....	43
Figure 42: FEM analysis of wishbone connector during braking.....	44
Figure 43: Milling of connectors	44
Figure 44: Verification of tool path using graph plot on the Fanuc computer	44
Figure 45: Tie rod assembly	45
Figure 46: Left tie rod on suspension seen from beneath.....	45
Figure 47: Front left wheel well on the final body shell	46
Figure 48: The final clevis design. Purple highlights the vibration damping bushings	46
Figure 49: FEM analysis of clevis	47
Figure 50: Clevises attached to wheel well using wedges and bushings	47
Figure 51: Motor wheel, 3D front and back view	49
Figure 52: Exploded view of completed motor assembly	50
Figure 53: Cross section of motor.....	50
Figure 54: Close up of the motor hub.....	51
Figure 55: 3D view of the new motor axle	52
Figure 56: Load cases for an axle during cornering.....	52
Figure 57: FEM analysis of motor axle subject to a hard bump.....	53
Figure 58: FEM analysis of motor axle on inner wheel of a typical, sharp curve	53
Figure 59: FEM analysis of motor axle on outer wheel of a typical, sharp curve	53
Figure 60: Outer and inner rotor with colorized magnet arrays.....	54
Figure 61: FEM simulation of separation using 3 holes	55
Figure 62: FEM simulation of separation using 4 holes	55
Figure 63: Deformation from separation, 6.2 cm max.....	56
Figure 64: Stresses from separation, 405 MPa max.....	56
Figure 65: Deformation from separation, 4.1 cm max, using alternative conditions...57	57
Figure 66: Stresses from separation, 166 MPa max, using alternative conditions	57
Figure 67: Close up of rim adapters, in green and blue. The yellow section is the rotor spacer	58
Figure 68: The new test adapter	59
Figure 69: Race track map for Shell Eco-marathon 2012 [15].....	72

1. Introduction

Shell Eco-marathon is a fuel-efficiency competition for engineering students held in three regions of the world: America, Europe and Asia. The competition places a great emphasis on using the least amount of energy to traverse a set number of laps on a closed circuit race track.

NTNU has competed in the European Shell Eco-marathon every year since 2008 with the car *PureChoice*. *PureChoice* was powered by hydrogen and arrived at second place in the fuel cell class. The year after (2009) it was renamed to *DNV Fuel Fighter* as part of the main sponsor change, and went to set the world record. In 2010 the team constructed a novel motor built into one of the rear wheels. Problems with the motor forced that team to return home with no valid result. The 2011 team, which I was a part of for my specialization project, sought to regain the edge and prove to DNV that NTNU was still worth the sponsorship. Improvements to the motor, electronics, suspension and aerodynamics lead to second place even though the weight of the car had increased significantly since the first year of 2008.

This year changes everything as the newest team has worked very hard to constructing a new car and selling the concept to possible sponsors. DNV wished to remain the main sponsor and agreed to increase the budget to enable the production off a completely new car with the lessons learned.

The upcoming Shell Eco-marathon Europe competition for 2012 introduces some major changes by moving the race from smooth high-speed race tracks to city streets, which requires better performance from the suspension. This has been one of the numerous arguments used in the negotiations with the main sponsor, DNV, to increase the budget for the new car which has been named *DNV Fuel Fighter 2*.

Although speed is not the goal, the time requirement demands a certain minimum average speed at around 25 km/h. At this speed aerodynamics, rolling resistance and handling greatly affects the resulting efficiency. Both the old and the new car uses a carbon fiber monocoque made from three pieces: An upper and lower shell, and a bulkhead, glued together. One of the great improvements with the new monocoque is that the wheel wells are integrated and continuous parts of the lower shell.

1.1. The team

The 2012 team consists of 14 master students from different engineering disciplines, ranging from mechanical engineering and industrial design to project management and media. They, including myself, are:

- **Aksel Qviller**
Front suspension, hubs and axles, mechanical motor parts
- **Hans Gudvangen**
Rear suspension, coilovers and wheels
- **Håkon Johan Seiness**
Steering transmission and brake system, battery
- **Fredrik Vihovde Endresen**
Electric motor research and development
Designated reserve driver
- **Petter Thorrud Larsen**
Aerodynamics, strength analysis and production of body shell
- **Mats Herding Solberg**
Design of body and visual theme
- **Eivind Sæter**
Design of body and interiors
- **Itsaso Yuguero Garmendia**
Systems engineering
Designated driver
- **Ørjan Sjo**
Body shell materials and negotiating sponsorships for the production of the body
- **Aslak Brage Espeland**
Windshield wiper and door mechanics
- **Fariborz Ali Heidarloo**
Project manager
- **Benjamin Guthjar**
Cybernetics, control system

- **Oluf Tønning**
Systems engineering

- **Silje Skogrand**
Media and PR, clothes and events

- **A team from Byggelandsbyen in Experts in Team (EiT)**
 - Magnus Holmefjord
Trailer
 - Bernt Kaarigstad
Trailer
 - Anders Brekke
Telemetry
 - Amund Hov
Telemetry

1.2. Sponsors

To show the size and momentum of the project, this section presents the companies currently involved in the project, ranked in order of economic contribution. At the time of writing, the exact values of some sponsors are not known, as there is some guesswork involved for finding the true value where companies operate with reduced bills and only cite some of the costs. This overview should give a clear indication, though:

- **Det Norske Veritas, main sponsor**
Sponsor value: 600 000 NOK in direct financial aid
- **Transnova**
Sponsor value: 200 000 NOK in direct financial aid
- **Eker Design**
Sponsor value: About 160 000 NOK in production services
- **HPC**
Sponsor value: About 100 000 NOK in materials and production services
- **SmartMotor AS**
Sponsor value: About 50 000 NOK in materials and services
- **Altitec**
Sponsor value: About 15 000 NOK in materials
- **Gylling Teknikk AS**
Sponsor value: About 15 000 NOK in materials
- **ProNor AS**
Sponsor value: About 40 000 NOK in materials
- **SKF Norge AS**
Sponsor value: 10 000 NOK in materials
- **Re-Turn AS**
Sponsor value: About 5 000 NOK in materials
- **Jackon Isolasjon**
Sponsor value: About 5 000 NOK in materials

2. Front suspension

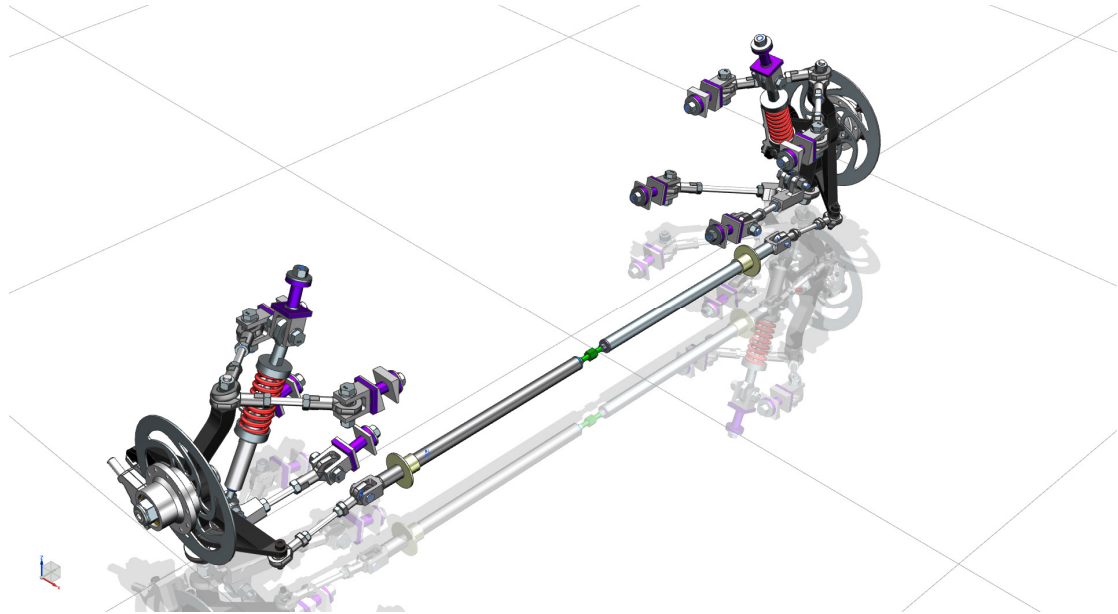


Figure 1: The final front suspension

2.1. Requirements

Before carrying out the design tasks, a number of requirements were specified in cooperation with other team members for all systems. These are the requirements for the front suspension, as listed in [1] with some additions for clarity. Also, the requirements laid out in the official Shell Eco-marathon do apply even though not listed explicitly here.

Table 1: Front suspension requirement specification

Requirement	Value	Must	Should
Scrub radius	<10mm	X	
Toe-in/toe-out	0°	X	
Camber angle	0°	X	
Caster angle	5°	X	
Correct Ackerman geometry with correct angle on toes		X	
Bump steer	0°/ cm	X	
Track width	≥ 100 cm	X	
Camber angle change during vertical travel	> ± 1 ° ≤ ± 2 °	X	
Damping/travel during race	> ± 1 cm ≤ ± 2 cm	X	
Damping/travel during race	> ± 2 cm ≤ ± 3 cm		X

Ground clearance with driver	≥ 10 cm	X	
Weight	< 2 kg	X	
Weight	< 1 kg		X
Adjustable toe-in/toe-out		X	
Adjustable Camber angle		X	
Adjustable Caster angle			
Adjustable height/ground clearance		X	
Vibration reduction		X	
Adjustable spring stiffness		X	
Adjustable damper coefficient		X	
Support bicycle-type hydraulic brake caliper		X	
Allow for lining of brake fluid pipes		X	
Easy to maintain		X	
Withstand lateral force caused by cornering	F_1	X	
Withstand longitudinal force caused by braking	F_2	X	
Withstand vertical force caused by weight of car plus driver, and g-forces	F_4	X	
Withstand torque from braking		X	
Turning radius	≤ 6 m	X	
Turning radius	≤ 4 m		X
Allow for lining of brake fluid pipes			X
Steering rotation must not bring wheels into contact with car body			X
Resist dive during braking (anti-dive)			X

For the modeling work and finite element analysis, it was decided to use UGS NX. All figures of 3D models and FEM simulations in this paper are made in NX, with the exception of the monocoque, which was imported from SolidWorks.

Also worth noting is that the wheelbase of the new car is 140 cm.

The top priority of the new suspension is not passenger comfort, but measures will be taken to reduce road noise from the tires, since this has been one of the recurring complaints. It is most important to keep all wheels in contact with the ground at all times for the sake of safety and fuel efficiency.

The aerodynamics, size and weight of the car's body has been prevalent during the design phase and overruled some of the design freedoms of the suspension. For instance, the diffuser underneath the new body is crucial for eliminating aerodynamic lift [1] and its geometry affects where the lowest mounting points for the suspension linkages can be placed. This means that an optimal roll center, placed as low as possible, cannot be achieved as the linkages will slant upwards into the body, especially for the rear suspension [1] where the diffuser slants up and away from the ground as it meets the car's tail.

Based on cost estimates made early in the fall of 2011, the front and rear suspension and steering was allotted a budget of 110 000 NOK.

2.2. Concept selection

The selection of the suspension concept was a difficult task, as we knew that adding features like damping would increase the weight, complexity and cost of the solution. The weight would most definitely increase if a solution with stiff linkages was chosen because the number of parts increases with the complexity, and that would also affect the design of the body to accommodate the suspension. Also, the behavior of a compliant mechanism [1], while elegant, is less predictable and by nature much less adjustable than jointed mechanisms.

Table 2: Trade-off matrix for front suspension concepts

		MacPherson		Double wishbone		Compliant mechanism	
Criteria	Weight	Score	Weighted score	Score	Weighted score	Score	Weighted score
Low weight	5	3	15	4	20	5	25
Adjustability	4	1	4	5	20	1	4
Manufacturability	3	3	9	4	12	3	9
Reliability	4	3	12	4	16	3	12
Low cost	4	2	8	1	4	2	8
Maintainability	3	3	9	4	12	2	6
<i>Weighted sum</i>		57		84		64	

The double-wishbone concept (with some variation in our implementation) was chosen in close cooperation with Gudvangen and Seiness as we felt most confident that this was a solution that we could deliver.

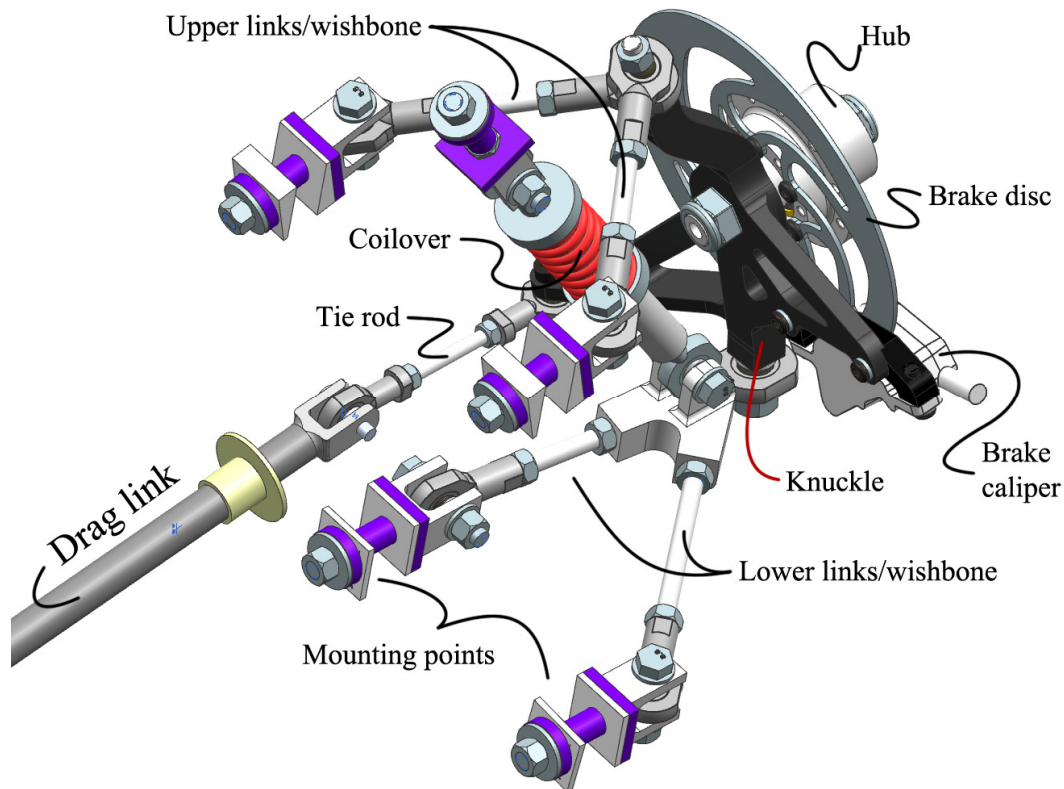


Figure 2: Double wishbone concept, parts annotated

2.3. Geometry optimization and force determination

In order to determine the forces attacking the parts and find the dimensioning criteria for the different parts, this section discusses the linkage geometry and then calculates the approximate resulting loads for key parts. During the projects progress, the design and analysis have been carried out in parallel, but it is more useful to present it here. Before the statics calculations the reasoning behind the geometry is explained.

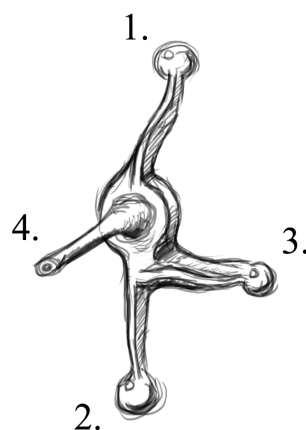


Figure 3: Typical steering knuckle concept

1. Top swivel joint
2. Lower swivel joint
3. Steering joint

4. Axle/hub

Figure 3 shows the parts that the steering knuckle must have in order to provide steering and spring action. The swivel joints allow the knuckle to rotate about its vertical axis to steer the attached wheel, but also the whole mechanism's up and down motion. The placement of these relative to each other are absolutely crucial to obtain the desired motion.

2.3.1. Camber change

When the car drives through a curve, the lateral acceleration will transfer weight to the outer wheels. With the ground as reference frame, the car will tilt to the side, and depending on the suspension kinematics, the wheels will alter camber angle. Since the camber angle both affects energy efficiency and lateral thrust force, the camber angle relative to the ground should remain fairly constant, or rather it should at least not become positive.

A positive camber angle means that we run the risk of developing less than required lateral force, with the possibility of slipping; and moving the contact point towards the center of gravity, which reduces cornering stability.

A negative camber angle would rather increase toppling stability, but could also lead to over steer. Also, with the car as reference frame, the negative camber change could be an unwanted effect of the car diving on the suspension as a result of braking or driving over bumps.

Since the car will be driven with a reasonably known weight, and the coilovers' lengths are adjustable, the ride height of 10 cm can be almost guaranteed, so that under normal conditions, the wheels will remain in neutral position so that the ground-to-camber-angle is correct.

With these considerations in mind, the solution chosen was to optimize the camber change for minimizing the ground-to-camber-angle during cornering action, with a negative result more desirable than positive, if non-zero. With an axle width of 100 cm, and a maximum delta change of ± 2 cm, the car's roll angle and the corresponding camber angle compensation can be calculated as follows:

$$\Delta\theta_{\text{camber,front}} = \arctan \frac{20\text{mm}}{500\text{mm}} = 2.29^\circ$$

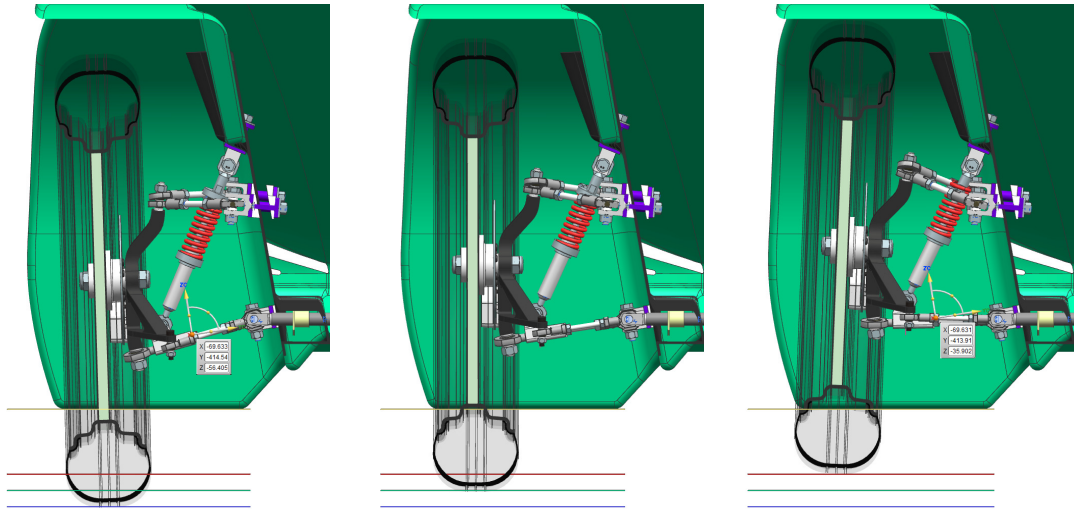


Figure 4: Camber angle change during spring action

The CAD assembly with its constraints was used to modify the link geometry until the desired camber angle change was achieved. A model with three sheets spaced 2 cm apart was made to show the different wheel positions during spring action when placed correctly beneath the shell model of the car. From left to right in Figure 4: Lowest (wheel hanging), ride height, highest (compressed by bump or hard braking or cornering).

2.3.2. Wishbone angles

Seen from above, the links form triangles that, coupled with the rod ends (section 2.7) and clevis mount points (section 2.8) as hinges, define the vertical swinging motion of the knuckles, and otherwise completely lock the knuckles from moving sideways or forward or backwards. The angle subtended (see Figure 5 and Figure 13) by the links in the horizontal plane determines the force absorbed during braking and cornering. The angles can be optimized for reducing stress during braking or cornering. The middle ground is 90° . However, to avoid the links interfering with the wheels turning about the steer axis, and because the car will corner harder and more frequently than braking, this angle was reduced to 80° .

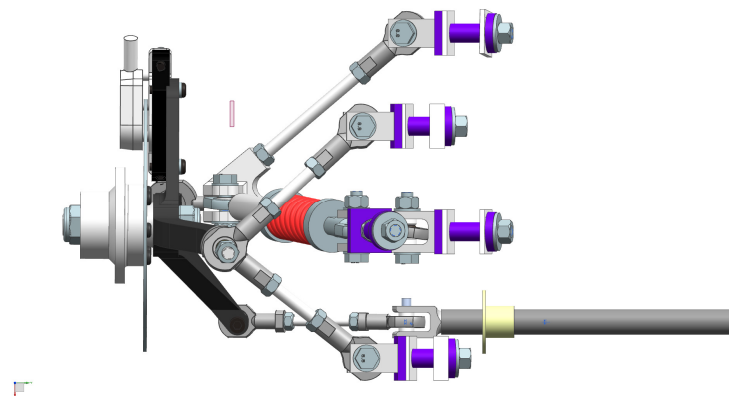


Figure 5: Top view of front left suspension links

For the lower links, the rear link had to be rotated and moved forwards to give space for the tie rods (Figure 6). Since energy efficiency and safety are so important, the no bump steer-requirement required that the tie rods be moved down into the plane of the lower links (Figure 7). The angle of the lower, rear link was thus reduced to 8° from the lateral axis of the car.

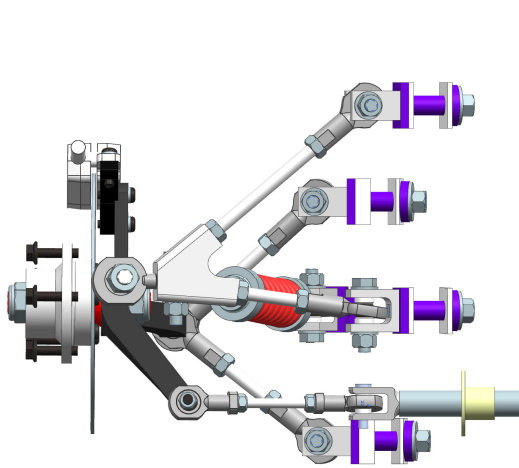


Figure 6: Viewed from beneath, front right suspensions

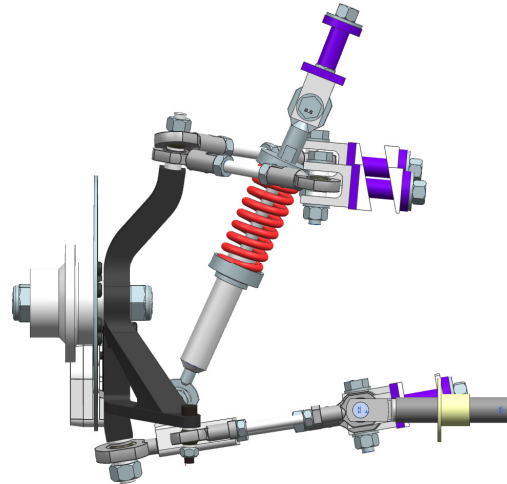


Figure 7: Rear view of front left suspension links

2.3.3. Calculation of link forces

The principal forces acting on the wheels that the suspension must support are derived and readily explained in [1]. They are presented here for the reader in the following figures:

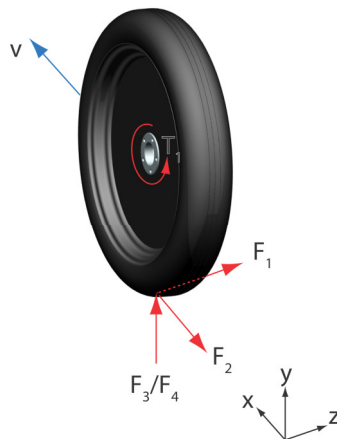


Figure 8: Forces acting on wheels [1]

Table 3: Dimensioning forces acting on wheels [from Gudvangen et al 2011]

Force	Value	Units	Description
P_1	510	N	Lateral force caused by cornering
P_2	550	N	Longitudinal force caused by braking
P_3	960	N	Vertical force acting on the engine wheel
P_4	780	N	Vertical force acting on the regular wheels

The P_1 and P_2 forces will be used to determine the forces acting through the primary linkages, and P_4 the force acting through the coilovers on the front suspension. To find these forces, the system(s) can be modeled as rigid bodies with loads and fixed constraints where the bodies are connected to other linkages or mounting points on the body.

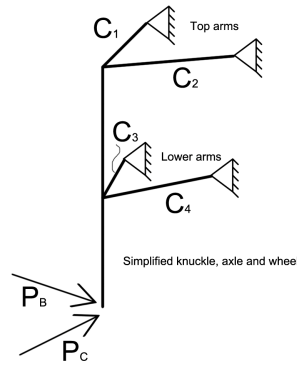


Figure 9: Rigid body model of front suspension, where P_B and P_C are the braking and cornering forces, and $C_{1,2,3,4}$ are the support forces acting through the wishbone links

The calculations are simplified by splitting the mechanical joints into three separate problems:

1. The steering knuckle experience longitudinal braking force or lateral cornering force
2. The top linkage triangles
3. The lower linkage triangles

This greatly simplifies the derivation of the constraint equations to be solved as a set of matrix equations. The steering knuckle can be modeled as a beam supported on two points where T_B is the torque generated from the braking force $P_B = P_2$, R_W is the wheel radius and L is the height of the knuckle:

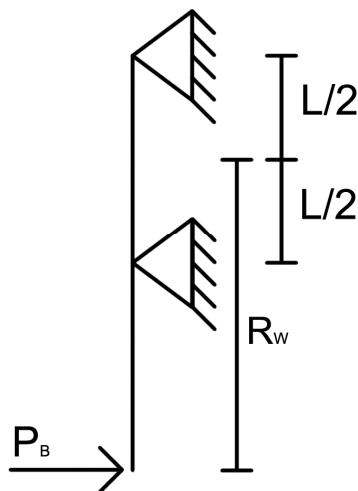


Figure 10: Force and constraints on the

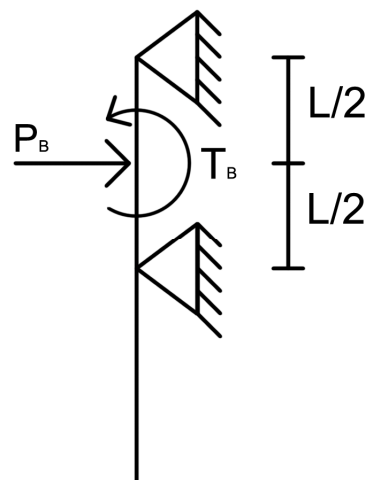


Figure 11: Simplified force and torque on

knuckle

knuckle

To further simplify the system, the reaction forces can be annotated so that the two unknowns for the knuckle are clearly shown:

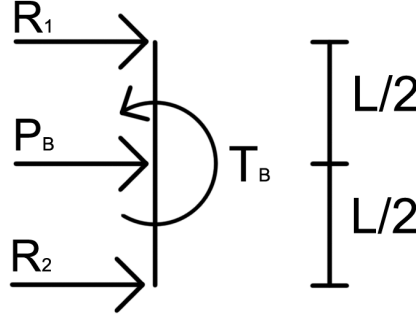


Figure 12: Steering knuckle modeled as a beam with load and reaction forces

This setup can also be reused when the effects of the cornering force are calculated. The system is then expressed as the following linear equations:

$$\begin{aligned} \Sigma F_X = 0 & \Rightarrow R_1 + R_2 + P_B = 0 & \Rightarrow R_1 + R_2 = -P_B \\ \Sigma M = 0 & \Rightarrow -R_1 \frac{1}{2}L + R_2 \frac{1}{2}L + T_B = 0 & \Rightarrow -R_1 \frac{1}{2}L + R_2 \frac{1}{2}L = -T_B \\ & & \Rightarrow -\frac{1}{2}L (R_1 + R_2) = -T_B \end{aligned}$$

In matrix form this gives:

$$\begin{bmatrix} 1 & 1 \\ -\frac{L}{2} & \frac{L}{2} \end{bmatrix} \begin{bmatrix} R_{B,1} \\ R_{B,2} \end{bmatrix} = \begin{bmatrix} -P_B \\ -T_B \end{bmatrix}$$

Thus, given that $P_B = P_2 = 550$ N, $R_W = 279$ mm and $L/2 = 100$ mm = 0.1 m:

$$T_B = P_B R_W = 550 \text{ N} \times 279 \text{ mm} = 154 \text{ N m}$$

$$\begin{bmatrix} 1 & 1 \\ -0.1 & 0.1 \end{bmatrix} \begin{bmatrix} R_{B,1} \\ R_{B,2} \end{bmatrix} = \begin{bmatrix} -550 \\ -154 \end{bmatrix} \text{N}$$

$$\Rightarrow \begin{bmatrix} R_{B,1} \\ R_{B,2} \end{bmatrix} = \begin{bmatrix} 1 & 1 \\ -0.1 & 0.1 \end{bmatrix}^{-1} \begin{bmatrix} -550 \\ -154 \end{bmatrix} = \begin{bmatrix} 0.5 & -5 \\ 0.5 & 5 \end{bmatrix}^{-1} \begin{bmatrix} -550 \\ -154 \end{bmatrix} = \begin{bmatrix} 495 \\ -1045 \end{bmatrix} \text{N} \quad ^1$$

Equation 1: Reaction forces on steering knuckle during braking

The top arms must thus exert a backwards force of 495 N and the lower arms a forwards force of 1060 N. To decompose these reaction forces into the arising axial forces in the top and lower links, the following model and equations are derived:

¹ These and the following equations were solved with GNU Octave, the matrix inverses are not typed out

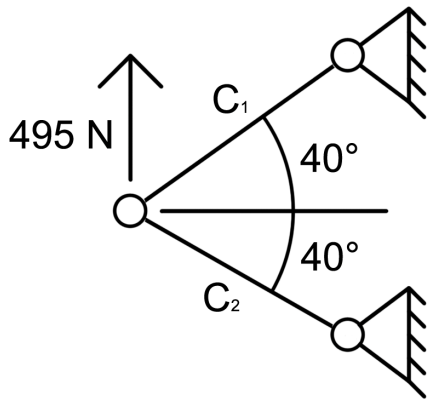


Figure 13: Constraint model for top arms during braking

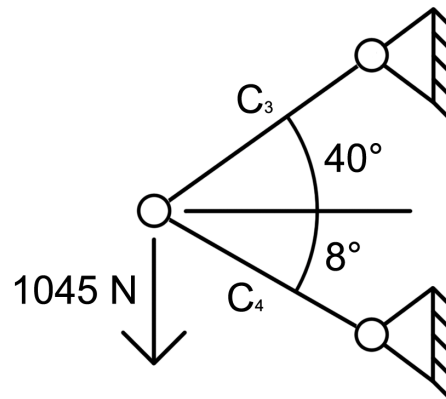


Figure 14: Constraint model for lower arms during braking

Solving for the support forces in the beams can be done with the following equation:

$$\begin{bmatrix} \cos \theta_1 & \cos \theta_2 \\ \sin \theta_1 & -\sin \theta_2 \end{bmatrix} \begin{bmatrix} C_u \\ C_v \end{bmatrix} = \begin{bmatrix} P_x \\ P_y \end{bmatrix}$$

Where P is the force acting on the swivel joint, C_u and C_v are the axial support forces in the beams, and θ_1 and θ_2 are the angles from the horizontal plane. Applied to the top arms this becomes:

$$\begin{bmatrix} \cos 40^\circ & \cos 40^\circ \\ \sin 40^\circ & -\sin 40^\circ \end{bmatrix} \begin{bmatrix} C_1 \\ C_2 \end{bmatrix} = \begin{bmatrix} 0 \\ -500 \end{bmatrix} \text{N}$$

$$\Rightarrow \begin{bmatrix} C_1 \\ C_2 \end{bmatrix} = \begin{bmatrix} \cos 40^\circ & \cos 40^\circ \\ \sin 40^\circ & -\sin 40^\circ \end{bmatrix}^{-1} \begin{bmatrix} 0 \\ -500 \end{bmatrix} = \begin{bmatrix} -389 \\ 389 \end{bmatrix} \text{N}$$

And applied to the lower arms this becomes:

$$\begin{bmatrix} \cos 40^\circ & \cos 8^\circ \\ \sin 40^\circ & -\sin 8^\circ \end{bmatrix} \begin{bmatrix} C_3 \\ C_4 \end{bmatrix} = \begin{bmatrix} 0 \\ 1045 \end{bmatrix} \text{N}$$

$$\Rightarrow \begin{bmatrix} C_3 \\ C_4 \end{bmatrix} = \begin{bmatrix} \cos 40^\circ & \cos 8^\circ \\ \sin 40^\circ & -\sin 8^\circ \end{bmatrix}^{-1} \begin{bmatrix} 0 \\ 1045 \end{bmatrix} = \begin{bmatrix} 1392 \\ -1077 \end{bmatrix} \text{N}$$

Here, a positive value means that the element undergoes tensile load, and negative values compressive loads.

For the cornering force, we observe that we can scale the result for the steering knuckle and avoid solving the same equations again:

$$P_1 = 510\text{N} = P_2 \frac{P_1}{P_2} = P_2 \times \lambda$$

$$\lambda = \frac{P_1}{P_2} = \frac{510}{550} = 0.9273$$

Using figure Figure 12 and Equation 1, the reaction forces on the steering knuckle become:

$$\begin{bmatrix} R_{C,1} \\ R_{C,2} \end{bmatrix} = \lambda \begin{bmatrix} R_{B,1} \\ R_{B,2} \end{bmatrix} = 0.9273 \times \begin{bmatrix} 495 \\ -1045 \end{bmatrix} = \begin{bmatrix} 459 \\ -969 \end{bmatrix} \text{N}$$

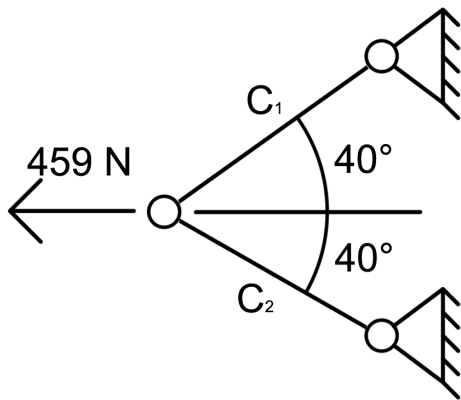


Figure 15: Constraint model for top arms during cornering

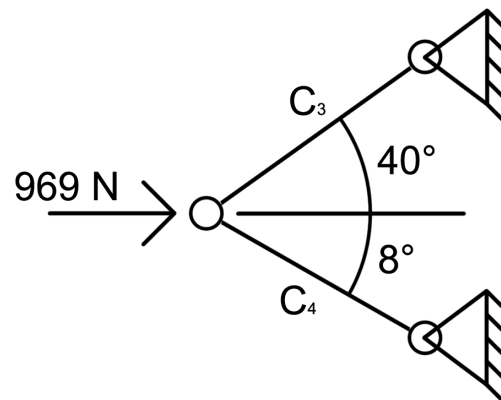


Figure 16: Constraint model for lower arms during cornering

$$\begin{bmatrix} \cos 40^\circ & \cos 40^\circ \\ \sin 40^\circ & -\sin 40^\circ \end{bmatrix} \begin{bmatrix} C_1 \\ C_2 \end{bmatrix} = \begin{bmatrix} 495 \\ 0 \end{bmatrix} \text{N}$$

$$\Rightarrow \begin{bmatrix} C_1 \\ C_2 \end{bmatrix} = \begin{bmatrix} \cos 40^\circ & \cos 40^\circ \\ \sin 40^\circ & -\sin 40^\circ \end{bmatrix}^{-1} \begin{bmatrix} 495 \\ 0 \end{bmatrix} = \begin{bmatrix} 323 \\ 323 \end{bmatrix} \text{N}$$

$$\begin{bmatrix} \cos 40^\circ & \cos 8^\circ \\ \sin 40^\circ & -\sin 8^\circ \end{bmatrix} \begin{bmatrix} C_3 \\ C_4 \end{bmatrix} = \begin{bmatrix} -969 \\ 0 \end{bmatrix} \text{N}$$

$$\Rightarrow \begin{bmatrix} C_3 \\ C_4 \end{bmatrix} = \begin{bmatrix} \cos 40^\circ & \cos 8^\circ \\ \sin 40^\circ & -\sin 8^\circ \end{bmatrix}^{-1} \begin{bmatrix} -969 \\ 0 \end{bmatrix} = \begin{bmatrix} -181 \\ -838 \end{bmatrix} \text{N}$$

For cornering in the opposite direction, the forces are inverted.

From these calculations we observe that the greatest axial loads in the links occur during braking, and the force of greatest magnitude (1392 N \approx 1.4 kN) will be used as

dimensioning criteria (with a safety factor) as it simplifies CAD modeling and manufacturing by reusing parts as much as possible.

2.3.4. Calculation of coilover forces

The force acting on the coilover due to the weight is illustrated below:

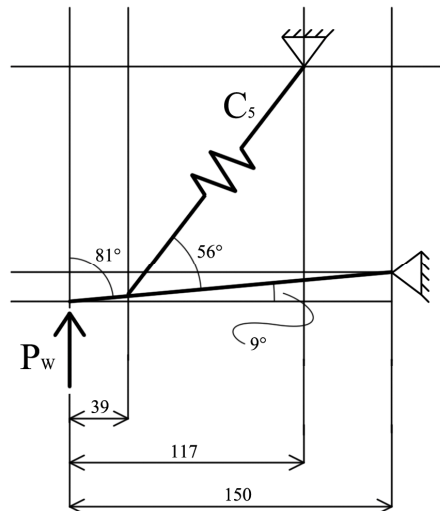


Figure 17: Diagram of weight force and link geometry view from behind the car, where P_w is the weight on the wheel and C_5 is the coilover's reaction force

Since $\cos 9^\circ \approx 1$ the calculation for the relation between the force P_w and C_5 becomes:

$$lC_5 \sin \varphi = -LP_w \sin \theta$$

$$C_5 = -\frac{LP_w \sin \theta}{l \sin \varphi} = -\frac{L \sin \theta}{l \sin \varphi} P_w = -\frac{150 \sin 56^\circ}{(150 - 39) \sin 81^\circ} P_w = -\frac{150 \sin 56^\circ}{111 \sin 81^\circ} P_w = -1.13 P_w$$

And with $P_w = \frac{1}{4} W = \frac{1}{4} \times 140 \text{ kg} \times 9.81 \text{ ms}^{-2} = 343 \text{ N}$ ²

$$C_5 = -1.13 P_w = -1.13 \times 343 \text{ N} = -388 \text{ N}$$

The negative sign indicates that the coilover undergoes a compressive load, or if it's unit vector points up to the right in the figure, it exerts a reaction force down to the left. As the wheel bounces up and down, the angles change and the multiplying factor will change too, however this value is useful for the coilover calculations.

2.3.5. Calculation of tie-rod forces

One of the load scenarios, which happened during the competition in 2011, is that the entire weight of the car lands on one of the front wheels during a less fortunate lift. The car is assumed to have a roll angle of 45° if this event should reoccur. To

² 140 kg was the estimated weight of the car with driver and equipment

calculate the force experienced by the responsible tie rod, the following criteria are set:

1. Car roll angle is 45° . The weight force is then multiplied by $\sin 45^\circ = 1/\sqrt{2}$
2. The caster angle is approximately 8°
3. The tie rod length is 72 mm

Since the ground-tire force is higher (about 71% of the car's weight, 971 N, compared to the cornering force of 510 N in section 2.3.3) than the cornering force, this will be the determining scenario for the tie rods.

The force on the tie rod occurs from the transfer of the force on the ground acting through the king pin axis to produce torque. The "Caster-length" is:

$$L_{caster} = R_W \tan \theta_{caster} = 279\text{mm} \tan 8^\circ = 39.2\text{mm}$$

The tie rod force follows from the torque:

$$140 \text{ kg} \times 9.81 \text{ ms}^{-2} \times \sin 45^\circ \times 39 \text{ mm} / 72 \text{ mm} = 526 \text{ N} \approx 0.53 \text{ kN}$$

As the wheel turns about the steering axis, the tie rod force will increase.

2.3.6. Anti-dive

The dive effect of the weight transfer towards the front when braking can be countered by exploiting the generated torque from the brakes to generate torque on the body that tries to lift the front up from the dive [10]. Experimentation with the top arm plane angle revealed that it affected the caster angle during spring action, which again influenced the steering-angle of the wheel, which again could adversely affect handling and fuel efficiency. The caster angle changes as a result of the top swivel joint moving forward or backwards, so that the tie rods change angle in the horizontal plane. Therefore, the anti-dive was reduced so that the caster change was negligible, while still trying to maintain some degree of anti-dive effect.

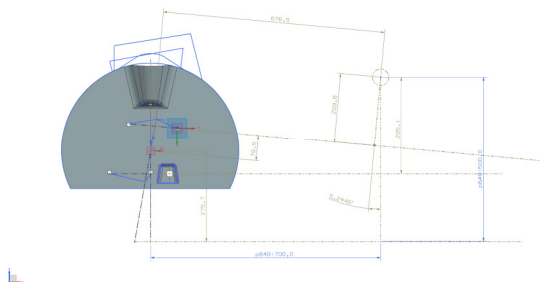


Figure 18: Sketch setup in NX to obtain measurements for anti-dive calculations

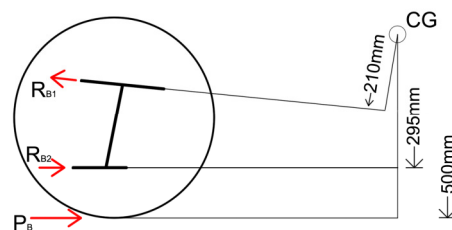


Figure 19: Force diagram of dive/anti-dive contributing forces

The knuckle reaction forces arising from braking, calculated in the previous section, can be used to estimate the resulting dive effect. The center of gravity of the car is assumed to be fairly low, namely 50 cm above the ground. Disregarding the anti-dive effect completely, the dive-torque from the front wheels braking is:

$$P_B \times 500 \text{ mm} = 550 \text{ N} \times 500 \text{ mm} = 272 \text{ N m}$$

By splitting up into torques arising from the lower and upper arms, this becomes:

$$T_{\text{dive}} = R_{B,2} \times 295 \text{ mm} = 1045 \text{ N} \times 295 \text{ mm} = 308 \text{ N m}$$

$$T_{\text{anti-dive}} = R_{B,1} \times 210 \text{ mm} = 495 \text{ N} \times 210 \text{ mm} = 104 \text{ N m}$$

$$T_{\text{tot}} = (308 - 104) \text{ N m} = 204 \text{ N m}$$

From this it can be concluded that the non-horizontal plane of the top arms significantly reduce the dive effect³; but no more than a quarter. Although the anti-dive angle had to be reduced to avoid “bump steer”, some effect positively remains, and the design choice is verifiable. Unfortunately, it will not be possible to measure the effect of the anti-dive geometry once the test driving starts, as the mounting points cannot be moved.

2.4. Hubs

The hubs were made for easy installation of bearings, held in place by retaining rings.



Figure 20: Front and back view of the hub

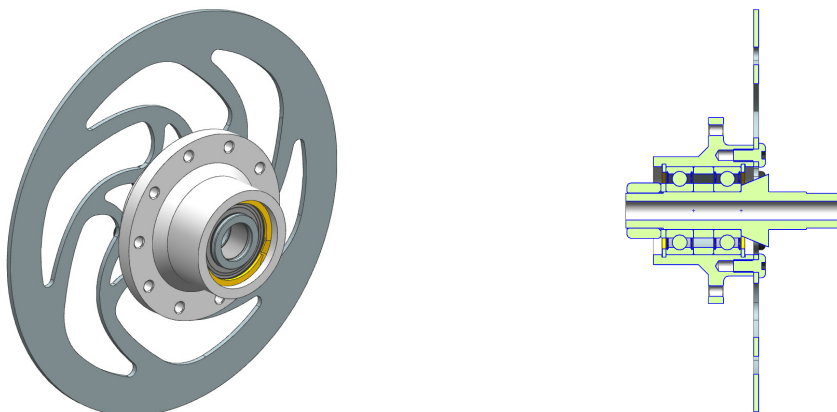


Figure 21: View of hub assembly

³ Anti-dive or anti-squat effects of the rear suspension are not taken into account.

The hub design sports a double set of lug bolt holes and brake disc holes. These extra sets of holes can be used as spares in case the threads should fail from wear or other accidents; plus, they save some (although minimal) weight. The five lug bolts concept was chosen over the previous center nut solution as it allows faster machining of the hubs, and no slow machining of large center nuts.

On recommendation from SKF, the internal hole tolerance was set to JS7 to allow a slight interference fit with the ball bearings to allow easy insertion and replacement.

FEM simulations were only done for braking and cornering, since the car's weight is transferred directly from the rims, through the hub, to the bearings.

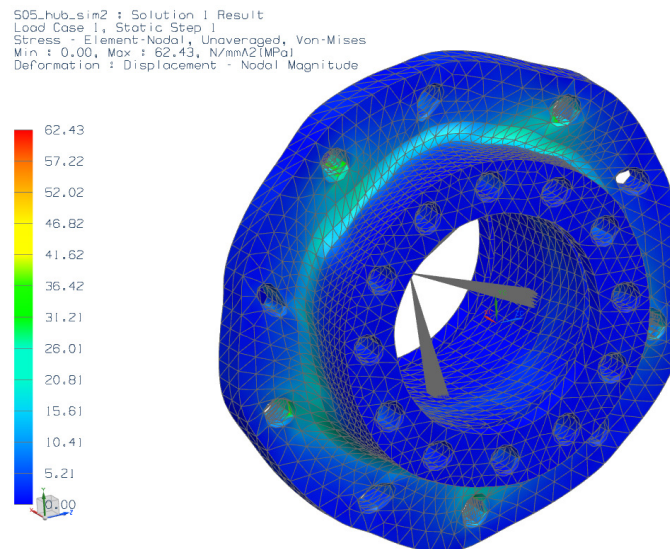


Figure 22: FEM analysis of hub during braking

The simulation of the braking situation shows that the stress concentrations stay below the fatigue limit of Alumecc 89, which is about 100 MPa [7].

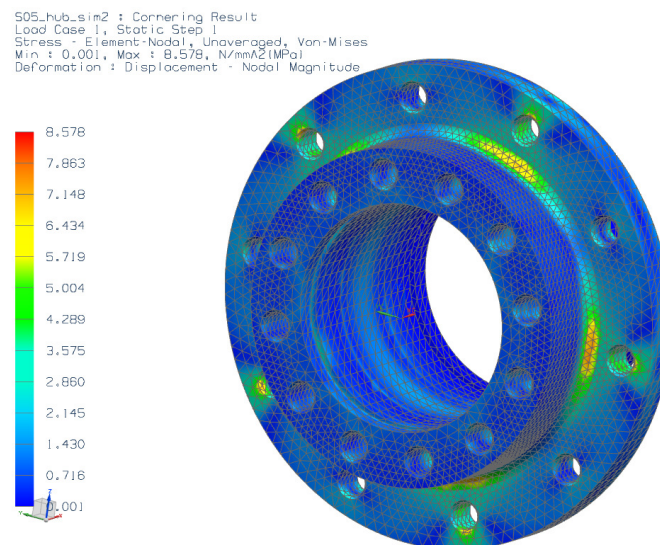


Figure 23: FEM analysis of hub during cornering

During cornering, the hubs undergo much lower stresses.

Three hubs were produced by NOMEK AS for about 6 700 NOK, including the material, Alumecc 89.



Figure 24: Hubs and coilover parts received from Nomek

2.5. Axles

The axles must also be sufficiently stiff to not elastically deform too much during operation, because the brake discs will begin to touch brake pads when not braking, which will be hard to compensate for. Since only the outer circumference of the cross section of a round bar significantly contributes to the stiffness, the axles could be made hollow to reduce weight without significantly reducing stiffness.

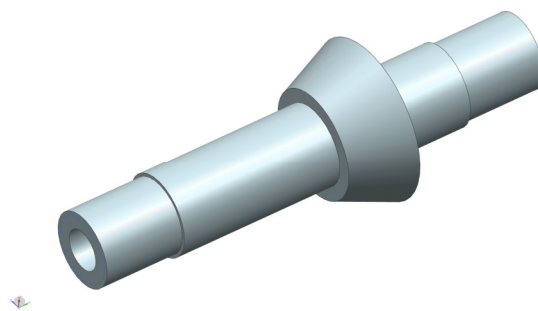


Figure 25: CAD model of axle

The axles are improved from the previous ones by using a large, conic flange to transfer the bending moment from the car's weight and braking to the knuckles.

S05_axle_sim1 : Cornering Result
 Load Case 1, Static Step 1
 Stress - Element-Nodal, Unaveraged, Von-Mises
 Min : 0.00, Max : 145.97, N/mm²(MPa)
 Deformation : Displacement - Nodal Magnitude

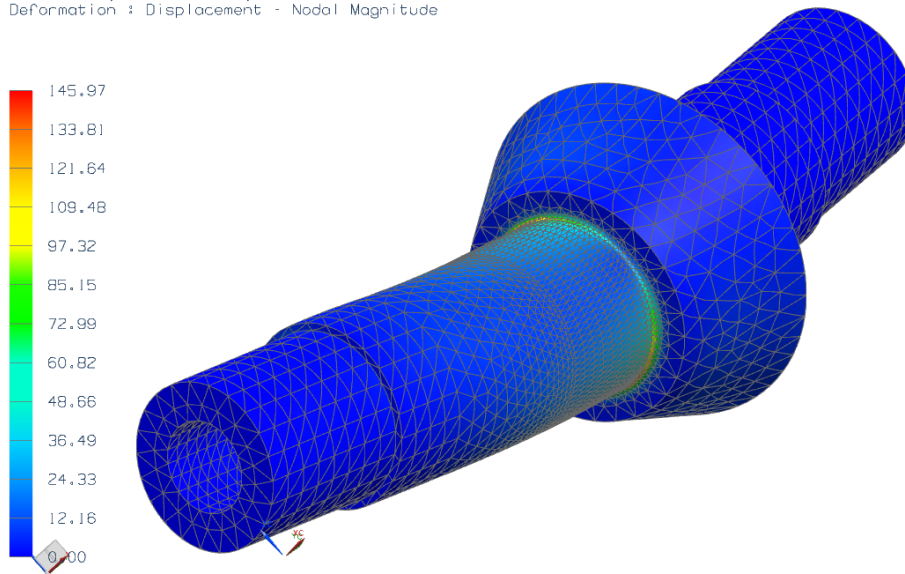


Figure 26: FEM analysis of axle during braking

The axle design was analyzed under the hardest braking scenario. Even though the maximum stress concentration climbs above the fatigue limit of aluminum, the ball bearings and spacers will help transfer loads to the face of the conic section, so the real stress concentrations are expected to be much lower. The deformation was so low (less than 0.1°) so the brake discs will not be affected.

The axles were produced by myself from a round bar of Alumecc 89.

2.6. Steering knuckles

A strong desire from the onset of the project was to use more carbon fiber in the suspension than before. The use of carbon fiber was strongly recommended by HPC, and would allow low weight given that carbon fiber has a density half of that of aluminum.⁴ The negative experience with magnesium alloy knuckles from 2011 [2] already excluded this option.

Carbon fiber composite parts are often shell-shaped and differ from the more massive solids usually made in metal, due to the anisotropic properties of composites. However, the steering knuckles will still require a rather massive piece, as Figure 3 shows:

One of the strong arguments for massive carbon fiber was that less material would go to waste in the production. If the knuckles were to be made in aluminum, they could either be sintered (additive) or machined from a solid block; both of which are expensive, and the latter leaves a *lot* of expensive waste material. Casting aluminum

⁴ Carbon fiber: 1.45 g cm⁻³,
 Aluminum alloy: 2.67-2.83 g cm⁻³
 Magnesium alloy: 1.7-1.8 g cm⁻³ (figures from HPC and CES EduPack, respectively)

would raise the cost even higher because of the molds required. The carbon fiber would rather be cast on a rough mould, and then later be machined into the final shape (Figure 35). As seen in Table 4 this is where the carbon fiber solution gains advantage over metal.

Table 4: Trade-off matrix for steering knuckle material selection

Criteria	Weight	Aluminum		Massive carbon fiber	
		Score	Weighted score	Score	Weighted score
Low weight	5	4	20	5	25
Adjustability	4	1	4	1	4
Manufacturability	3	4	12	4	12
Reliability	4	5	20	4	16
Low cost	4	2	8	3	12
Maintainability	3	4	12	3	9
<i>Weighted sum</i>			76		78

2.6.1. Ackerman steering

Ackerman steering is necessary to accommodate the smaller turning radius that the inner steering wheel subtends compared to the outer wheel. The behavior has been closely scrutinized in the CAD models for the new front suspension, as this was one of the goals from the onset. Although the formulas for calculating the angle of the toes can be easily derived⁵, experiments showed that this does not necessarily lead to a satisfactory solution.

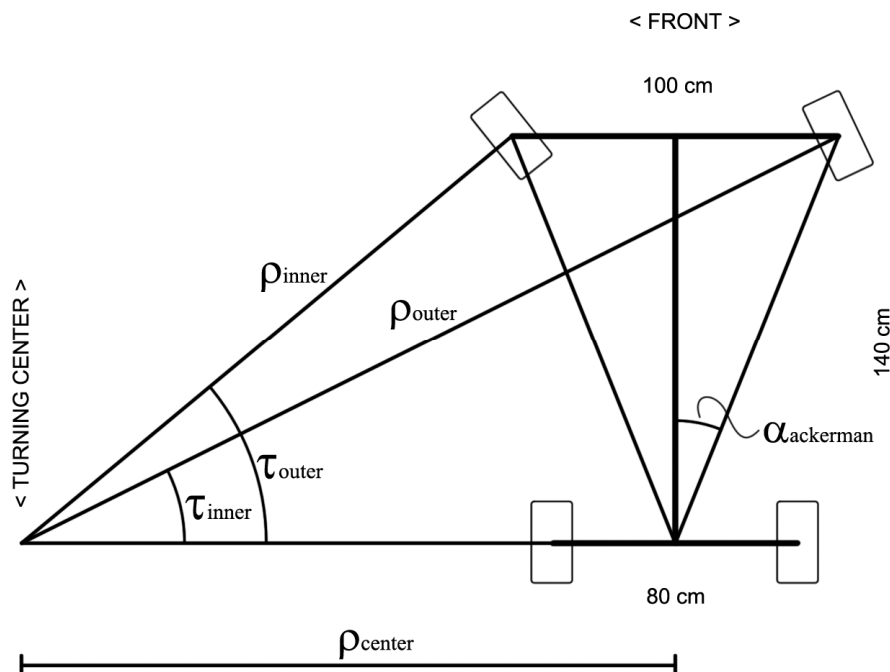


Figure 27: Ackerman steering based on sketch in the PD-journal, wheels and angles annotated. α is the typical toe-angle when driving straight ahead.

⁵ Ackerman steering sketches and calculations can be found in the PD-journal

This mode of analysis has two goals:

1. Ensure satisfactory ackerman steering
2. Ensure a turning radius of 6 m (as required by Shell Eco-marathon) or less

The exact requirements for the steering angles was not well documented in the literature studied. The Ackerman steering geometry is only optimal at low speeds when the tires develop little to no lateral forces. At higher speeds the behavior changes, the turning center moves forward [10].

According to [8], full ackerman is not necessary: They discovered that a Ferrari F40 only used “40% of theoretical full ackerman was used, to no obvious detriment on full lock; no squeal could be heard on a polished floor, the steering remained light and the car stayed easy to push around.”

With purely mechanical, passive steering – no active hydraulics controlling the steering angles of each wheel independently – it is not possible to achieve full ackerman steering throughout all wanted turning radii. A test setup in NX showed that the steering appears fully ackerman compliant the first few degrees, and then the difference increases progressively until the inner wheel massively over-steers. This over steer of the inner wheel is thought to be good, since the lateral acceleration of the car (at higher speeds) transfers weight to the outer wheels, but as there will be some scrubbing it may waste energy. Still, given that we have been provided with a map of the race track with annotations of the corners, we know that the corners are no less than 15 m at the sharpest, and 20 m in most other corners. The ackerman test model was thus used to optimize the position of the toes on the steering knuckles to achieve optimal ackerman on these curve radii.

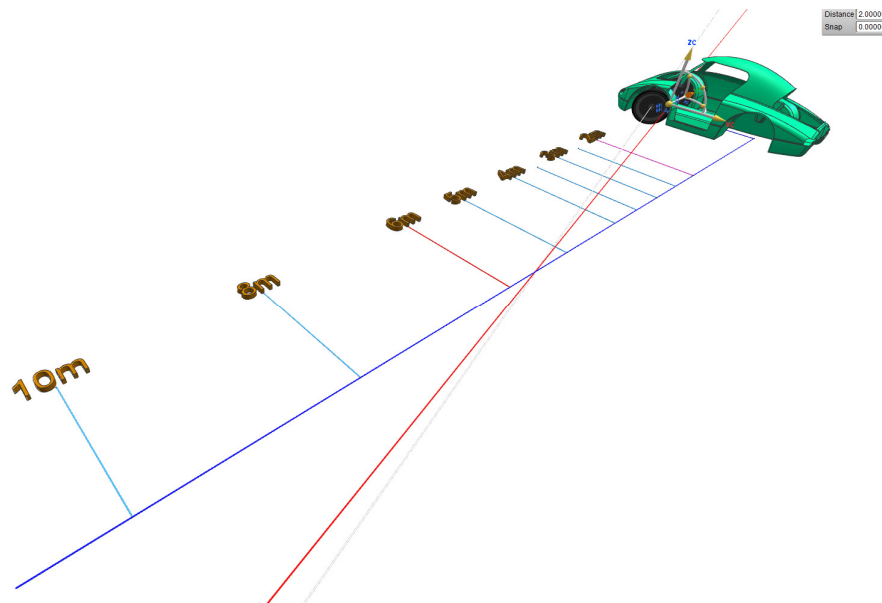


Figure 28: 3D view of steering radius check

As seen in Figure 28, the grid marks the position of the different turning radii from 2 to 25 m, with the most important ones annotated. The red bar is an extension of the right axle, and the white of the left axle, so that the turning center can be observed as

the drag link is moved in the CAD assembly, exploiting the constraints on all the suspension parts.

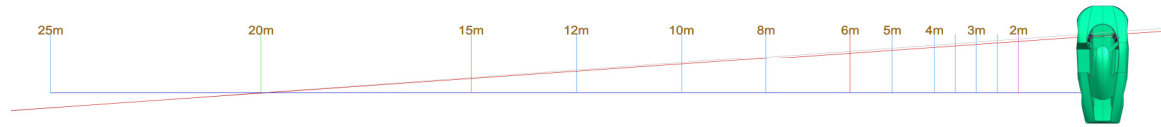
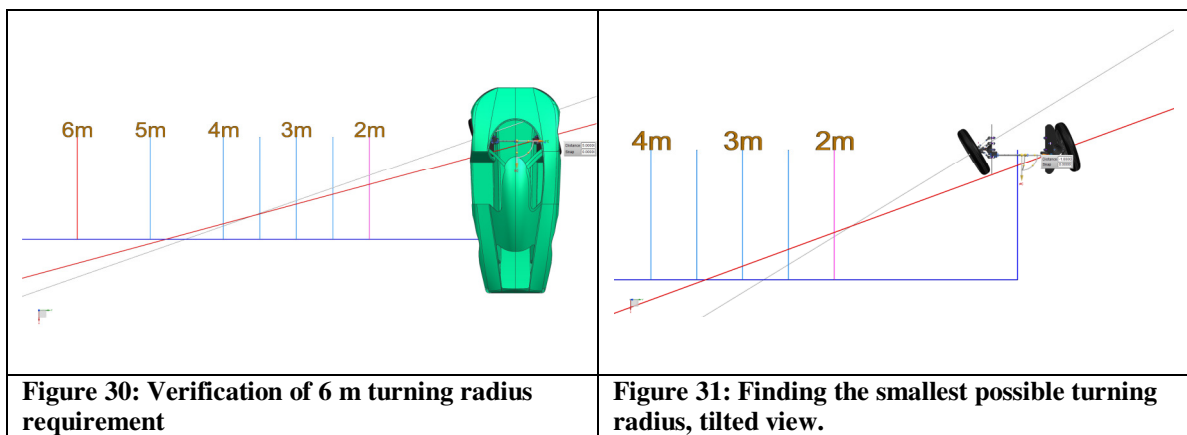


Figure 29: Verification of ackerman steering for 20 m turning radius

Figure 29 demonstrates the goal of satisfactory ackerman steering for cornering radii common on the race track. The testing showed that, as expected, the angles can be tuned by modifying the length of the drag link and tie rods, and the angle of the toes. The next figures, Figure 30 and Figure 31, shows the verification for smaller turning radii.



This method of testing was indispensable and much easier to deal with than manually calculating the steering angles.

2.6.2. Strength

The steering knuckles would be impossible to analyze using shells and laminates. Instead, an isotropic model was analyzed for braking and cornering scenarios where the results can give an indication of the forces that must be absorbed by the massive laminate.

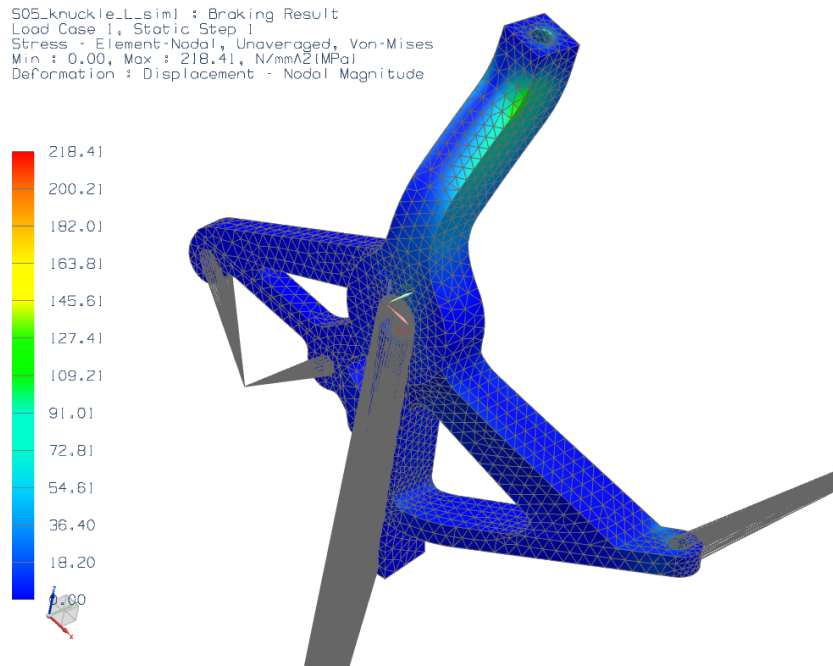


Figure 32: FEM analysis of knuckle during braking

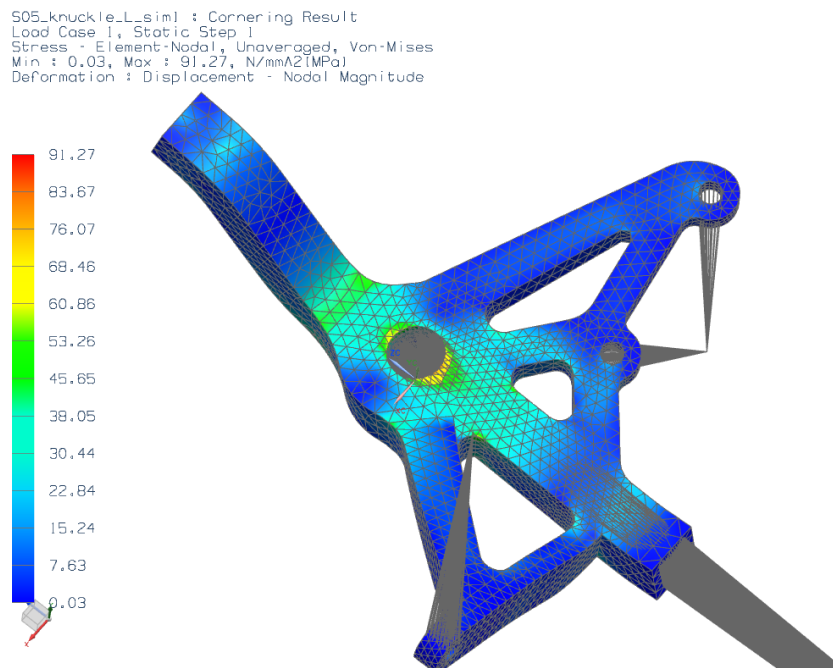


Figure 33: FEM analysis of knuckle during cornering

The stresses revealed by these simulations are far below the strength of the DB 420 carbon fiber.

HPC provided 15 mm thick samples of massive carbon fiber for testing. The results are documented in [13]. The tests revealed that the bolt connections would require reinforcement to avoid delamination. This reinforcement could be made using unidirectional carbon fiber wrapping as illustrated in Figure 34. Otherwise, our tests showed that a bolted connection could withstand as much as 9 kN [13], far exceeding the required 780 N specified in section 2.3.3.

2.6.3. Production of steering knuckles

The knuckles were to be produced from the same material as the monocoque, a carbon fiber type known as DB 420 with $+45^{\circ}/-45^{\circ}$ fiber directions, as large quantities of this material were brought in for an affordable price by the team members working on the production of the body. The exact properties of this material were unfortunately not known; the theoretical properties are listed in section 6.2.

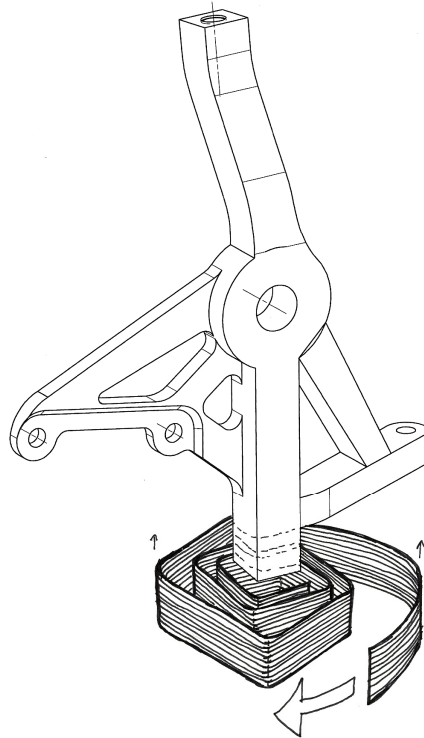


Figure 34: Unidirectional carbon fiber wrapping for reinforcement of bolted connections

HPC suggested that they would cast and cure blocks of carbon fiber shaped by a mold, which we would then post process by milling into the final shape. Figure 35 explains the production technique. The mold was machined from Ebaboard 60 in the Prototype lab and sent to HPC for employment.

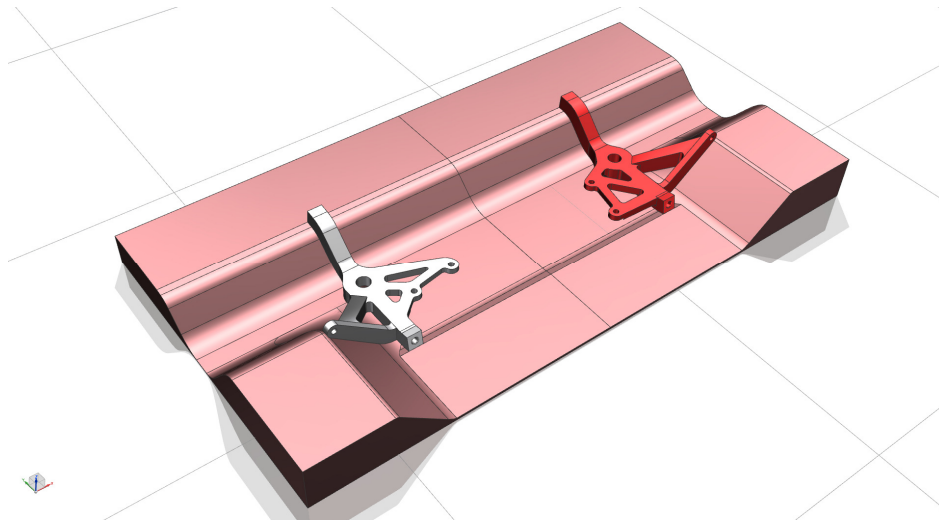


Figure 35: Mold for carbon fiber knuckles

At the time of writing we were waiting for the material for the knuckles (both front and rear) to arrive from HPC. Only two raw pieces for the rear suspension had arrived already. Enough material will be delivered for a double set of knuckles for both the front and rear suspension, so there is room for experimenting with the reinforcement. The price for each “slab” was 1 500 NOK

2.6.4. Milling of carbon fiber

Based on Børge Holen’s advise; diamond-coated end mills were used for machining the massive carbon fiber into the final shape of the steering knuckles.

Two Ø8 mm diamond-coated solid end mills were purchased from Seco Tools AS with a 25% discount with a total price of approximately 2 600 NOK. The delivered products were actually Ø10, but were put into use anyway for milling the rear knuckles first. They were also used to carve out the monocoque’s bulkhead.

Reidar Frog in Bergbygget workshop was consulted for carbon fiber machining advice. Accordingly, the dust-like chips from the machining of carbon fiber composites, apart from all inhalation, is not as dangerous as machining some forms of pure graphite where the particles may be small enough to diffuse through the skin.

The actual milling was scheduled to be done by Bjarne Stolpnæssæter with the CNC mill in the Prototype lab. In addition to proper vacuuming and safety glasses, a set of double-layer coal-filter respirators were purchased from Clas Ohlson to protect the persons working with the machining. The breathers remove more than 99.95 % of airborne particles as small as solvent vapour, which suffices to protect from the comparably larger carbon fiber composite chips, or dust. The people working with carbon fiber machining also used gloves and sleeves as the small chips irritate the skin. Still, for long-term high volume production the workers should probably be physically separated from the work pieces.

2.7. Linkages

The linkages were found to be easiest to make by using standard parts. With the sponsorship agreement with SKF, and leftovers from earlier project teams, the required number of rod ends could be afforded. Similar types of rod ends are also commonly used on real cars. Variations of male and female and mixed rod ends on the different links were considered, however the rod type link with external threads (Figure 36) is the easiest to make and therefore the approach taken. The links' adjustability comes from using threads with opposing handedness in each end. SKF offers rod ends with both right- and left-handed threads.

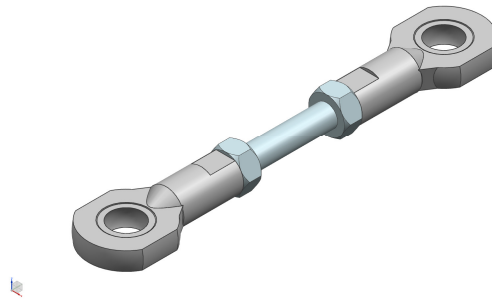


Figure 36: Link consisting of rod ends and nuts

2.7.1. Link strength

The link rods are easily machined from round bars, and 24 meters of Ø10 mm Aluminum 6082 T6 were purchased from Smith Staal AS at an economic price of about 50 NOK per 6 meter. It was unjustifiable to use anything thinner than Ø8 mm for the primary links and Ø6 mm for the tie rods. The strength of the rods is determined by the strain diameter from the thread size:

$$d_s = (d_2 + d_3) / 2$$

Where d_2 and d_3 are the pitch and minor diameter of the threads [4].

For external M8 and M6 these are [19]:

Table 5: Table of minimum pitch and minor diameters of ISO M6 and M8

Thread size	M6 (mm)	M8 (mm)
d_2	5.212	7.212
d_3	4.596	6.596
d_s	4.904	6.904

$$A_{\text{strain, M6}} = \pi r^2 = \frac{\pi d_s^2}{4} = \frac{\pi (4.904 \text{ mm})^2}{4} = 18.89 \text{ mm}^2$$

$$A_{\text{strain, M8}} = \pi r^2 = \frac{\pi d_s^2}{4} = \frac{\pi (6.904 \text{ mm})^2}{4} = 37.44 \text{ mm}^2$$

For wrought Aluminum 6082 T6, the fatigue strength is minimum 90 MPa [18]. The fatigue limit of the links using M6 and M8 are thus:

$$F_{M6} = 90 \text{ MPa} \times 18.89 \text{ mm}^2 = 1700 \text{ N} = 1.7 \text{ kN}$$

$$F_{M8} = 90 \text{ MPa} \times 37.44 \text{ mm}^2 = 3370 \text{ N} \approx 3.4 \text{ kN}$$

This exceeds the max link force calculated in section 2.3.3 (1.4 kN for links, 0.53 kN for tie rods) by factors of 2.43 and 3.2, respectively. The safety factor criterion has thus been satisfied.

Even though left-hand threads are common on bicycles, it was difficult to obtain taps and dies for making them. A set of left-hand taps and dies for M6 and M8 were purchased from Tess Trondheim AS, and the delivery time was about 5 weeks.

One other failure mode to be considered is buckling. The Euler buckling criterion for beams with plain joints that don't exert bending moment is given by:

$$P_B = \pi^2 EI / L^2 \quad [3]$$

where L is the length, and E and I are Young's modulus and area moment of inertia. The modulus of elasticity for aluminium 6082 T6 is 70 GPa, The longest link is 116 mm and the tie rods are 108 mm long. Thus, the area moment of inertia for the tie rods and the longest link mm rods are:

$$I_{polar} = \pi d^4 / 32 \quad [3]$$

$$I_{tie\ rod} = \pi (6 \text{ mm})^4 / 32 = 127.24 \text{ mm}^4$$

$$I_{link} = \pi (8 \text{ mm})^4 / 32 = 402.12 \text{ mm}^4$$

$$P_{tie\ rod} = \pi^2 \times 70\ 000 \text{ MPa} \times 127.24 \text{ mm}^4 / (108 \text{ mm})^2 \approx 814 \text{ kN}$$

$$P_{link} = \pi^2 \times 70\ 000 \text{ MPa} \times 402.12 \text{ mm}^4 / (116 \text{ mm})^2 \approx 2400 \text{ kN}$$

While these results exceed the requirement by far, they do not account for ductile fracture which will occur long before loads of these magnitudes can be attained.

The maintenance-free rod ends with "steel/sinter bronze composite" of SKF's rod ends were chosen for their lack of play and ability to run without lubrication. The second choice would be rod ends requiring maintenance, but these have some play between the rod head and the ball which is undesirable as it can introduce vibrations and misalignment. Analyses of the suspension setup show that as little as 0.5 mm elongation or contraction of a link affects the wheel angles.

The rod ends with 8 mm bore (SI 8 C), easily support up to 5.85 kN, and 3.6 kN for 6 mm bore rod ends (SI 6 C), which exceed the required loads calculated the previous sections.

Even though the double-wishbone concept was chosen for both the front and rear suspension, the end result was a variant of multi-link suspension. Only the lower swivel joints need a rigid part to connect the coilover, so the top swivel joint was made easier to manufacture by splitting it into two coaxial rod end joints located next to each other. The effect of two off-plane joints was found to be negligible and thus carried forward.

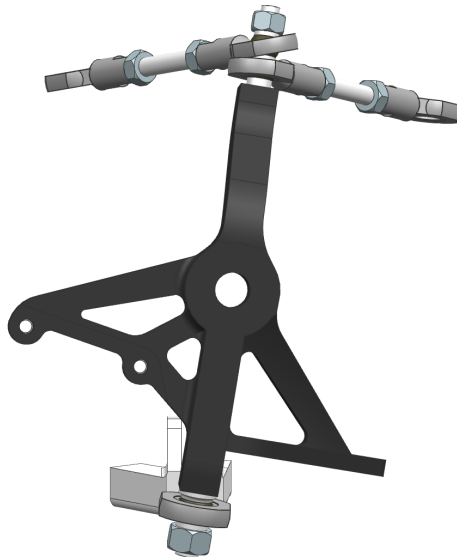


Figure 37: Single rod end on bottom, double rod ends on top

2.7.2. Wishbone connectors

For the lower control arms, two solutions were considered. While a single-piece solid wishbone (Figure 38) is simpler, it is not adjustable like the connector with rod links (Figure 39). The connector solution is also easier to manufacture.

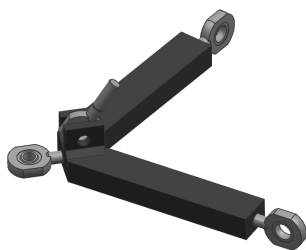


Figure 38: Solid lower wishbone

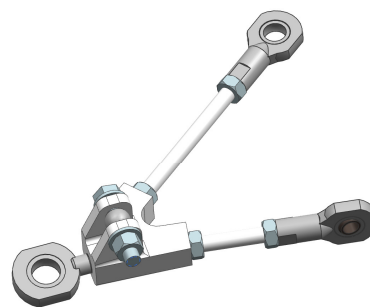


Figure 39: Connector and link rods

The lower control arms of the suspension can be made adjustable and lightweight by using a small “wishbone connector” that rigidly connects the lower swivel joint, the lower links and coilover.



Figure 40: 3D views of the left wishbone connector

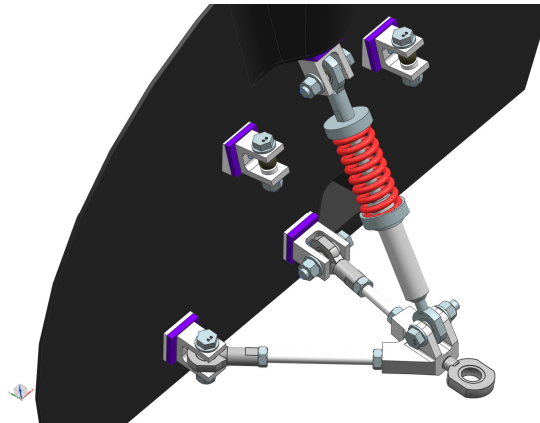


Figure 41: Left suspension with connector and coilover

The wishbones for the left and right sides are symmetrical.

The rod ends from SKF are primarily meant for radial loads (relative to the eye). While the old PureChoice/DNV Fuel Fighter car has successfully used 8 mm plain spherical bearings to carry the car's weight before, the size of the lower rod ends was increased to 10 mm.

The permissible load for rod ends is given by SKF as

$$P_{\text{perm}} = C_0 b_2 b_6 \quad [16]$$

where

- C_0 = static load rating [kN]
- b_2 = temperature factor (= 1.0 for temperatures below 120 °C)
- b_6 = load type factor (= 1 for constant, 0.5 for alternating)

Additionally, SKF states that “*the load portion acting perpendicular to the direction of the shank axis should never exceed the value of 0.1 C_0 .*” [16] Thus the weight carrying capacity of SI 8 C and SI 10 C bearings are given by:

$$P_{\text{perm},8} = 12.9 \text{ kN} \times 1.0 \times 0.5 \times 0.1 = 645 \text{ N}$$

$$P_{\text{perm},10} = 18.3 \text{ kN} \times 1.0 \times 0.5 \times 0.1 = 915 \text{ N}$$

With an expected vertical load of 780 N (section 2.3.3) it can be verified that 10 mm bore rod ends should be chosen over the other.

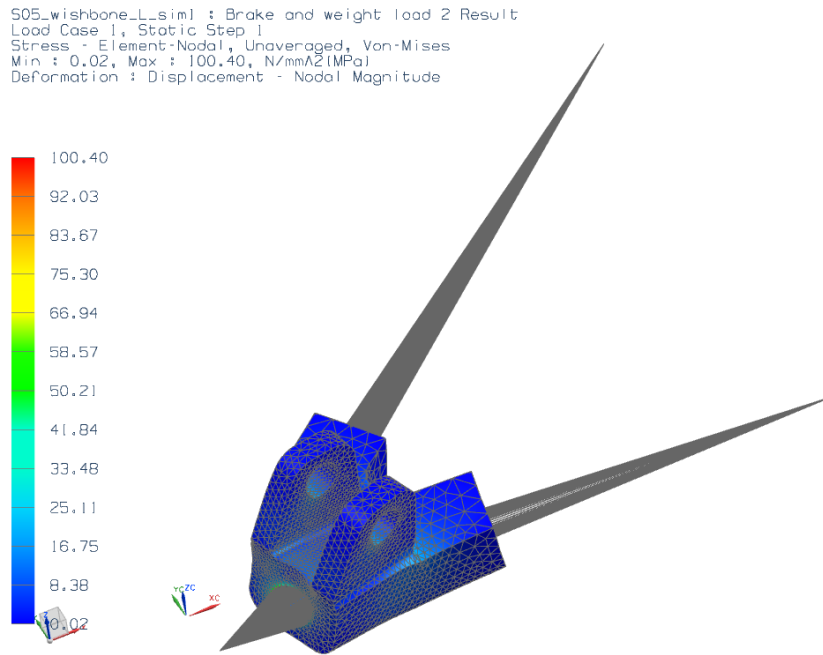


Figure 42: FEM analysis of wishbone connector during braking

The figure above shows the FEA of a connector during the hardest possible braking. The stress concentrations approach 100 MPa, which is at the limit of aluminum. Since this load scenario rarely will occur, the design is approved.

The wishbone connectors were milled from Alumec 89 with the Makino CNC machine in IPM's workshop⁶. Børge Holen provided an unused 10 mm solid end mill with 2.5 mm end radius for machining aluminum.

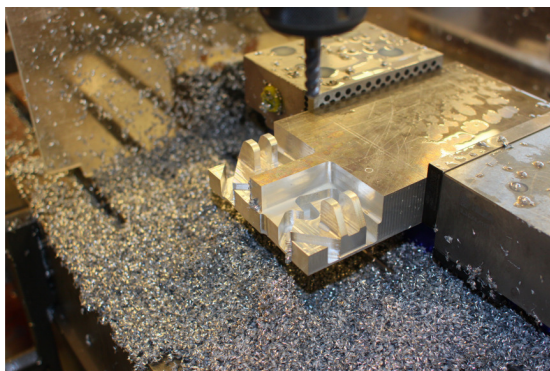


Figure 43: Milling of connectors

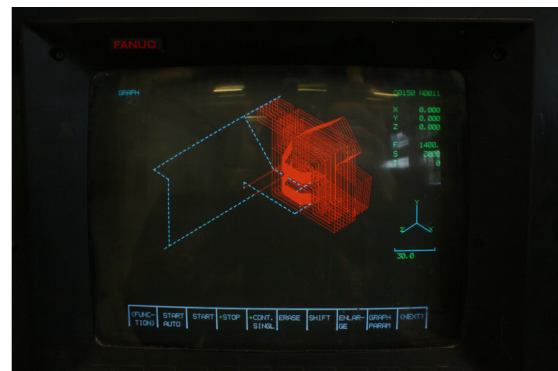


Figure 44: Verification of tool path using graph plot on the Fanuc computer

⁶ The G-code programming is listed in section 0

2.7.3. Tie rods

The previous tie rods of the old car used an SKF rod end on the outer end, and a plain spherical bearing to connect with the drag link. Since the latter one only offers up to 13° of tilt, this was not enough for the new geometric layout. In cooperation with Seiness, working on the steering transmission, the solution was changed to use the same type of rods as elsewhere on the suspension, only smaller. The Ø6 mm rods with right-/left-hand threads in either end allowed for adjustability and unobstructed spring- and steering action of the front wheels.

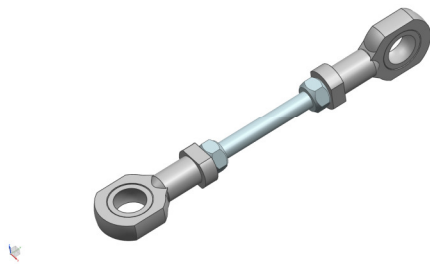


Figure 45: Tie rod assembly

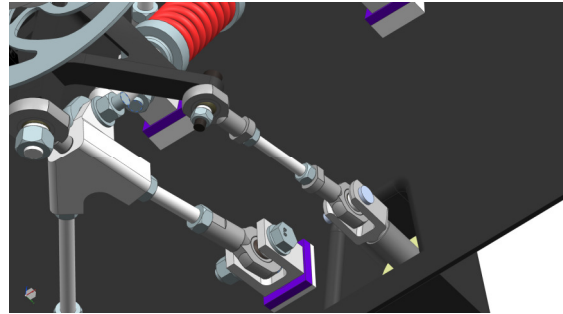


Figure 46: Left tie rod on suspension seen from beneath

2.7.4. Roll- and strut bar

A roll bar was considered, but this would increase the weight (which was already a critical issue), and add a more complex joint mechanism for retaining the roll bar in the wheel wells made us avoid this feature. As roll bars affect the over/under steer factor [5], this is an option we retain as a backup solution in case the car should severely under- or over-steer.

Using a strut bar was also considered, but the stiffness of the monocoque was so high that this would be unnecessary weight. The dashboard, being designed by students undertaking Engineering Design and Materials Technology in fourth grade, will likely help stiffen up the wheel wells because of its load carrying capacity for the steering wheel.

2.8. Mounting points

Each wheel requires five mounting points: Four for the links controlling the spring action motion, one for the coilover, and one extra for the tie rods. On the rear suspension the tie rods are connected directly to a sixth mounting point in the wheel well, while on the front they are connected to the drag link. Initially the plan was to make the wheel wells completely flat for easy production. The wheel wells were already slanted to optimize for camber angle changes (which also acted as release angles for releasing the cured shell from the mold), but HPC recommended to reshape the wells into something more reminiscent of the strut towers on real cars, to attach the coilovers. The resulting shape helps stiffen the shell.

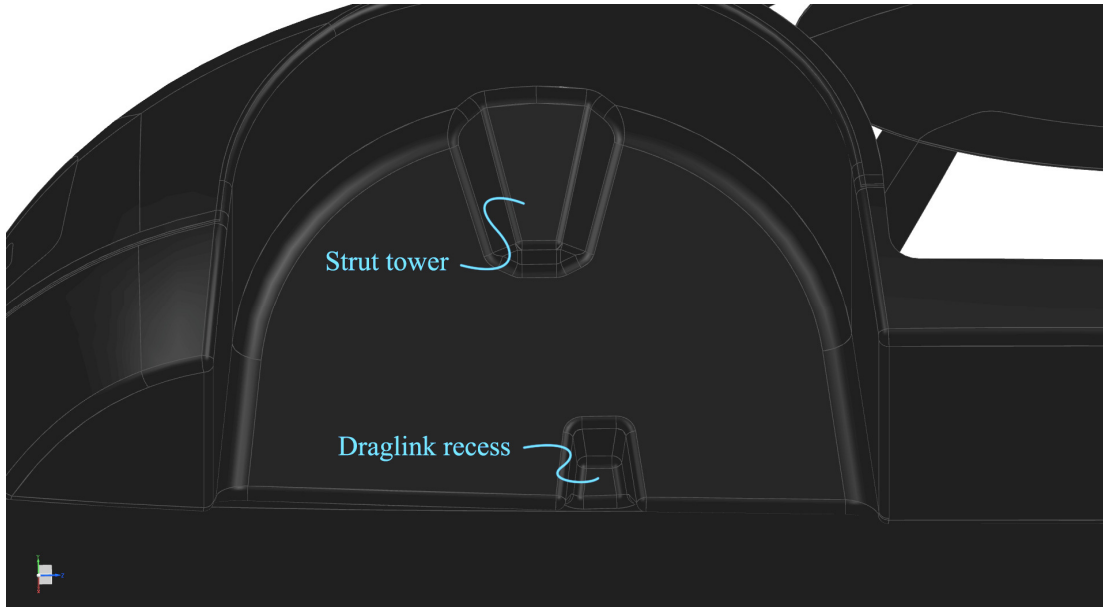


Figure 47: Front left wheel well on the final body shell

A recess which the drag link could move into, and bring with it the tie rod joint was also incorporated. The reason is that the draglink-tie rod-joint must lie in plane with the other mount points when driving straight ahead (as shown in Figure 4) to avoid bump steer, and to enable maximum steering deflection, the joint might have had moved through the well if this recess was not there.

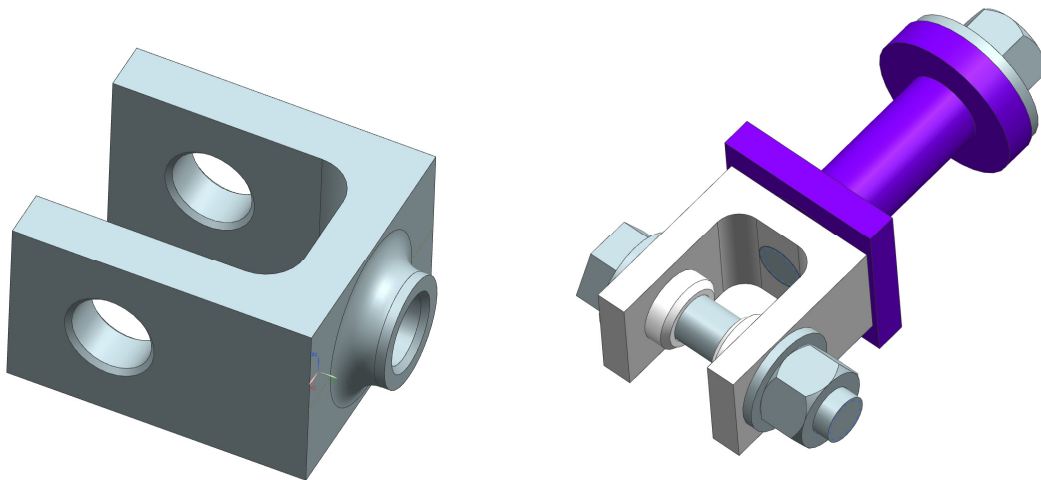


Figure 48: The final clevis design. Purple highlights the vibration damping bushings

The clevises were designed to be lightweight, easily machined and allow maximum rod end tilt. Since H7 reamers are the only affordable tools to finish the holes holding the transverse bolts, and the internal clearance of the rod ends is smaller, the concept was simplified to use an ordinary partially threaded bolt.

The bolt connecting the clevis to the body will be glued into the clevis so that a nut next to the clevis is not required (but the nut on the inside of the car will still be needed).

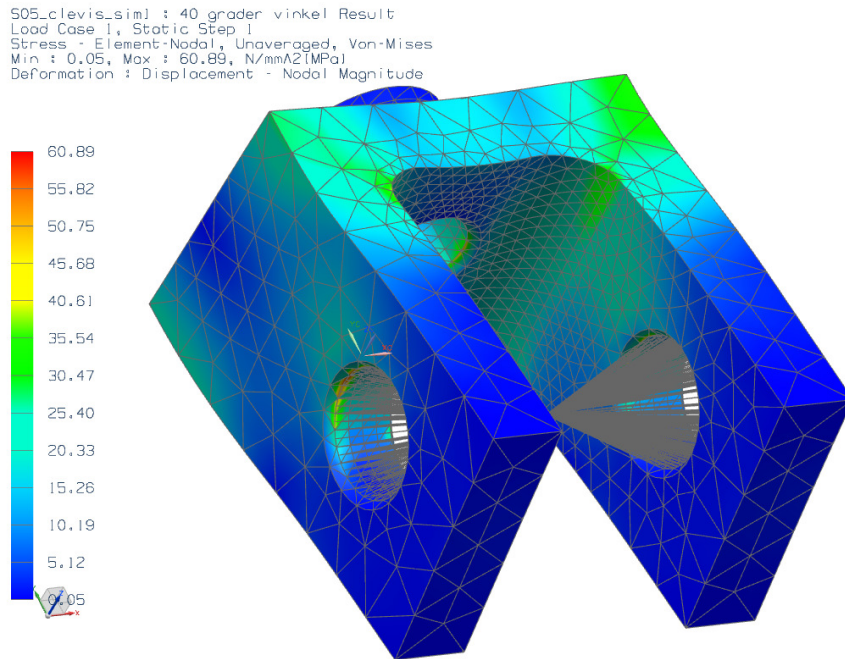


Figure 49: FEM analysis of clevis

Stress analysis shows that the maximum stress concentration in a clevis is just 61 MPa, which gives a safety factor of 1.6 with regards to the fatigue limit (90 MPa). In real life, the tensile preload on the bolt will reduce the stress concentrations since friction will absorb some of the forces.

The slope of the wall in the wheel wells makes it difficult to attach the clevises with the right angles. To work around this problem, without complicating the design of the clevises, wedges. Since these wedges only undergo compression (and the pressure is low), the range of materials to select from expands into polymers which are lighter than metal.

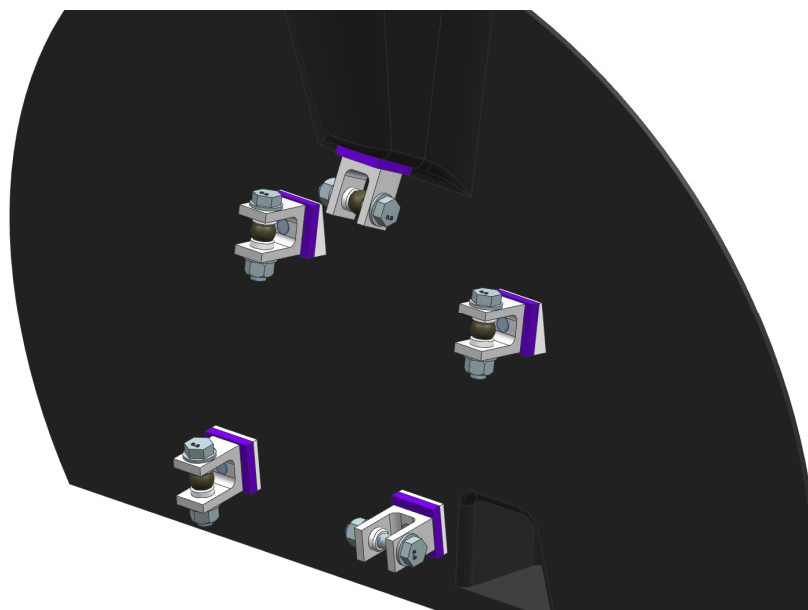


Figure 50: Clevises attached to wheel well using wedges and bushings

A casting resin, RenCast CW 2215 and hardener, with compressive strength 80-90 MPa [17], was purchased from Lindberg & Lund for 424 NOK to cast the wedges. For the vibration damping, Flexane 60 was also purchased from Lindberg & Lund for 670 NOK. These parts, the wedges and vibration dampers, had to be cast in molds from Ebaboard 60.

3. Motor design

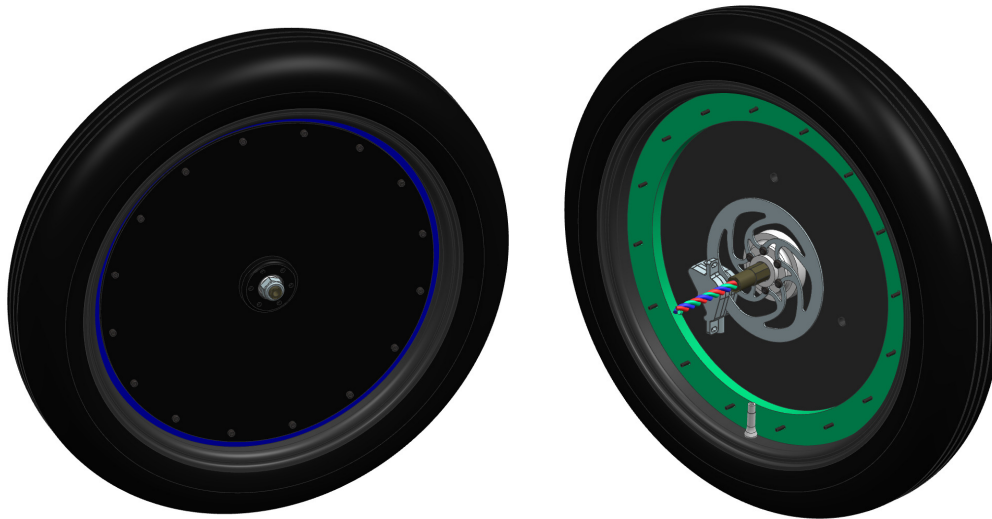


Figure 51: Motor wheel, 3D front and back view

This section summarizes the work I did on the mechanical motor parts. It is an improvement of last year's motor based on the specifications by Fredrik Endresen, which again are based on the work of Lubna Nasrin.

3.1. Requirements

Table 6: Requirements specification for mechanical motor parts

Requirement	Value	Must	Should
Withstand lateral force caused by cornering	F_1	X	
Withstand longitudinal force caused by braking	F_2	X	
Withstand vertical force caused by weight of car plus driver, and g-forces	F_4	X	
Withstand torque from braking		X	
Fit the engine rim		X	
Allow space for the three wires for the drive current		X	
Adjustable magnet air gap		X	
Non-magnetic material		X	
Support the strong magnet array	4000 N	X	
No parts interfere during rotation		X	
Separable		X	
Weight	< 10 kg	X	
Weight	< 7		X

The motor was allotted a budget of 100 000 NOK. In addition to service hours, SmartMotor sponsored the production of Endresen's magnets, which were expensive and had a lead time of many months. A significant improvement over the old motor is the use of a Hallbach array which eliminates the need for steel cores to conduct the magnetic flux and reduces the weight of the engine considerably – if the magnets are glued directly onto the rotors.

Due to the efficiency of the motor, combined with the low nominal output (around 100 W) alleviates the need for cooling, it is therefore not a requirement.

3.2. Concept description

In general the new motor is an incremental improvement of last year's motor, and its concept is therefore largely already determined. The design of the stator and magnet arrays and air gaps are Endresen's work. The stator is a resin cast with Litz wire windings cast inside. The axle is completely stationary and does not rotate, but the rotors attached to it do, and transfer the torque to the rim.

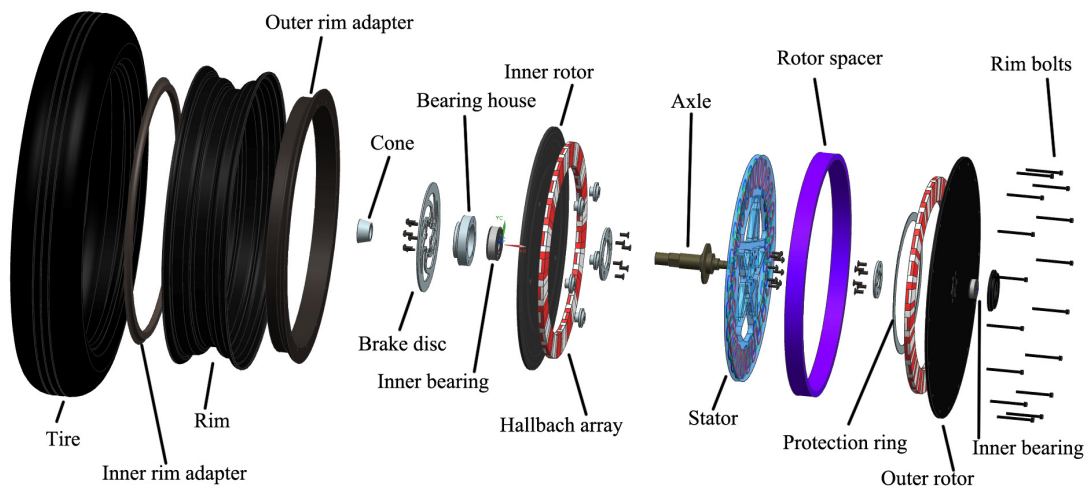


Figure 52: Exploded view of completed motor assembly

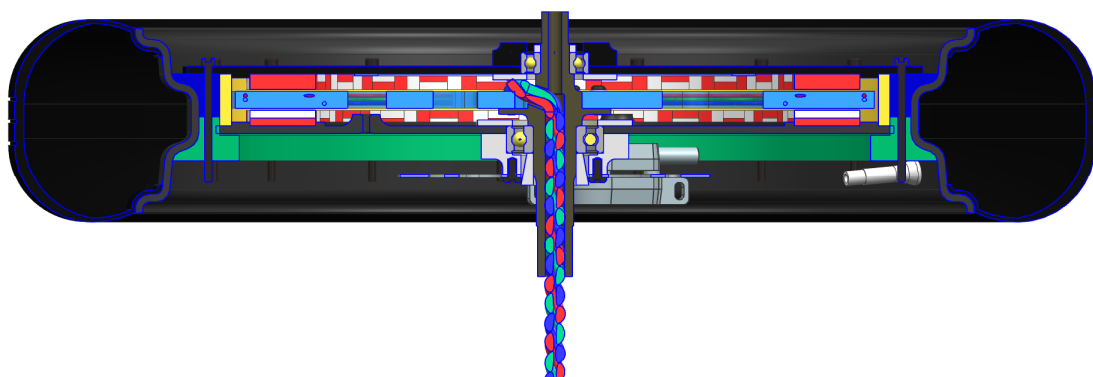


Figure 53: Cross section of motor

3.3. Hub and axle

The new magnet array, with the removal of the iron core rings used before by the 2011 and 2010 teams, the motor can be made much more compact. It is in fact now becoming so narrow that there were problems with making the hub compact enough. This was solved by using flat-head counter-sunk screws.

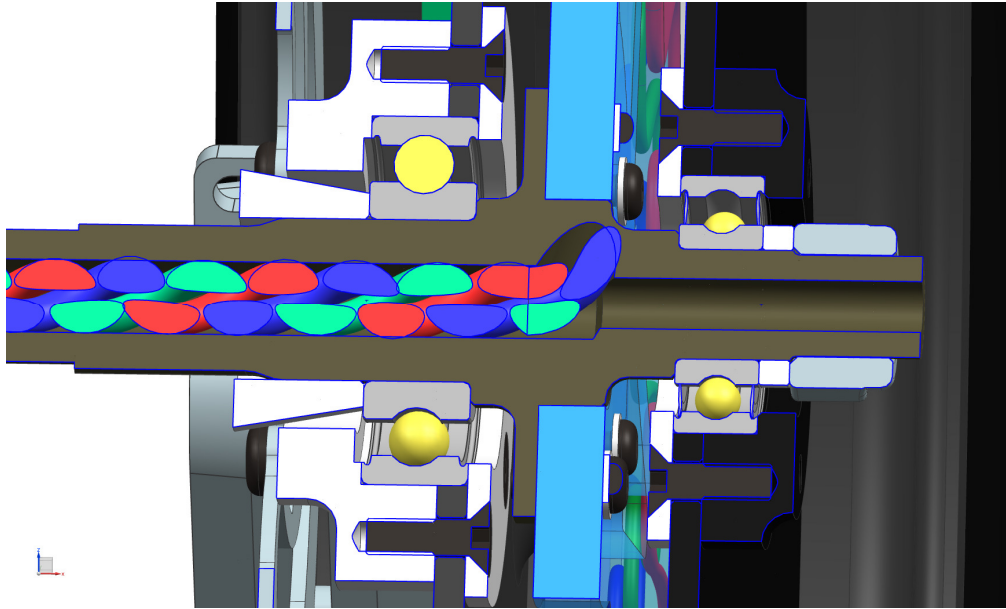


Figure 54: Close up of the motor hub

The axle sees a major improvement over the older axles. The first axle in the in-wheel motor (2010) consisted of a steel shaft with an aluminum flange seated with an interference fit to hold the stator cast in epoxy. The revision I made in 2011 for my specialization project increased the size of the shaft as much as possible without having to modify one of the existing stators from 2010 that were to be reused. The new axle of 2012 is further increased in diameter to accommodate easy insertion of wires for the three-phase drive current, but mainly for strength. It is, however, kept reasonably thin to avoid oversized and heavy bearings. The axle is also greatly simplified, from three pieces to hold the stator, into just a single axle with a large flange to hold the stator. This increases the amount of waste material since the axle has to be machined from a rod with larger diameter than previously, but the large motor budget allows such expenses.

The other improvement, enabled by the increased diameter, is the octagonal section that mates with the suspension. This will make it simpler to attach the motor wheel to the car as it does away with the key that easily fell out [2].

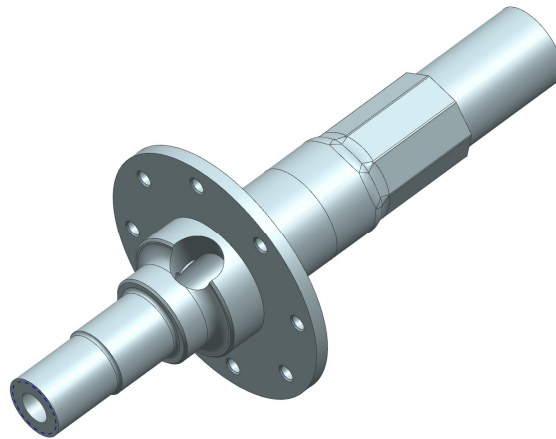


Figure 55: 3D view of the new motor axle

The motor axle will be used on the left side of the car, and as the sharpest turns go to the left, the motor axle will rarely undergo the extreme loads of hard cornering. The spreadsheet shown in section 0 was used to determine the forces applied to the inner or outer wheel of a typical curve. This is important because the lateral force developed in the contact patch is weak when it acts to further bend the axle, but when the force is strong due to turning in the other direction, the force acts to jack the car up and works to cancel the bending moment from the weight force (see Figure 56).

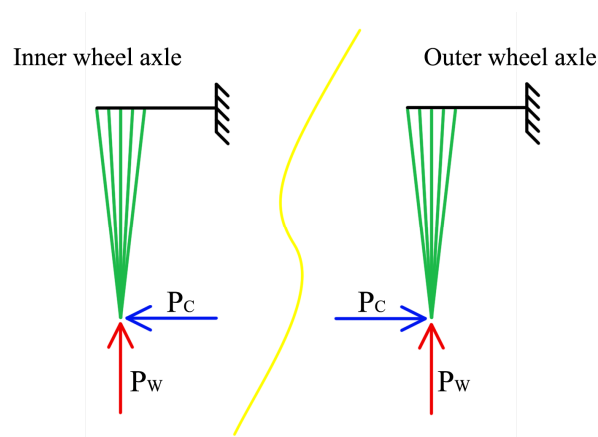


Figure 56: Load cases for an axle during cornering

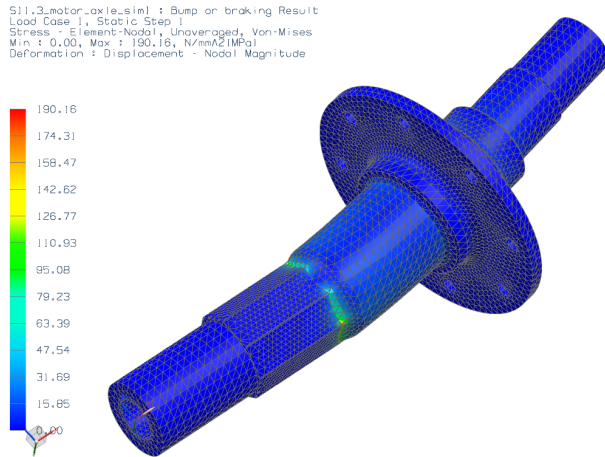


Figure 57: FEM analysis of motor axle subject to a hard bump

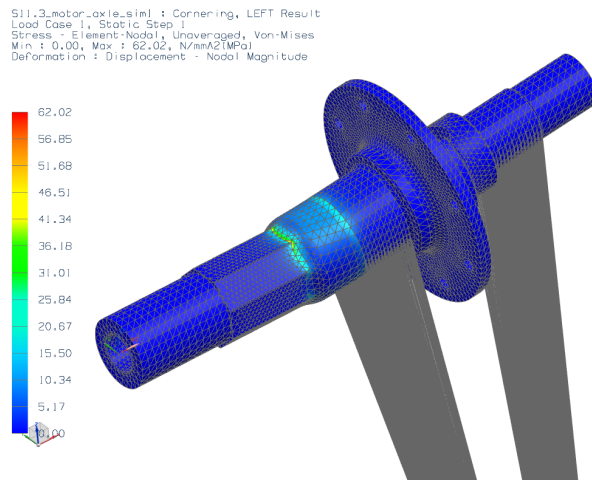


Figure 58: FEM analysis of motor axle on inner wheel of a typical, sharp curve

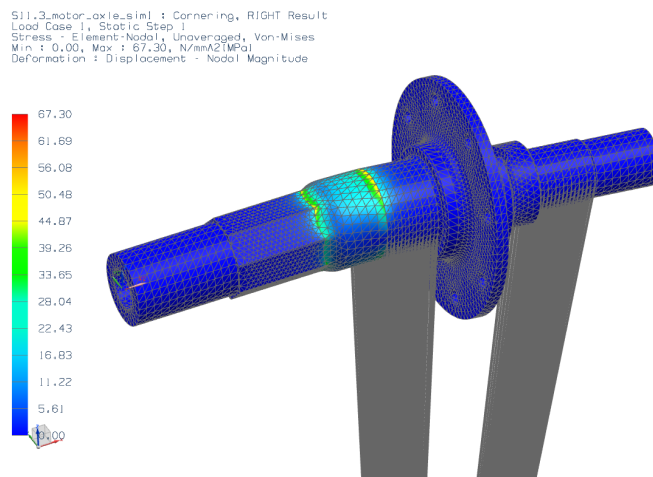


Figure 59: FEM analysis of motor axle on outer wheel of a typical, sharp curve

The simulations of the motor axle were performed without the support of the cone as the conditions were difficult to reproduce in NX. With the cone in place the stresses of 190 MPa from the bump simulation will be drastically reduced.

The axle was machined by Finmekanisk for 5 400 NOK, using Aluminium 7075 provided by the Department of Electrical Power Engineering.

3.4. Rotors

The rotors consist of one large circular plate with the magnet arrays glued on, a bearing and a housing which locks the bearing to the rotors. A smaller bearing is used for lower weight and friction on the outer rotor, where the axle is smaller since there are no wires going through this part of the axle.

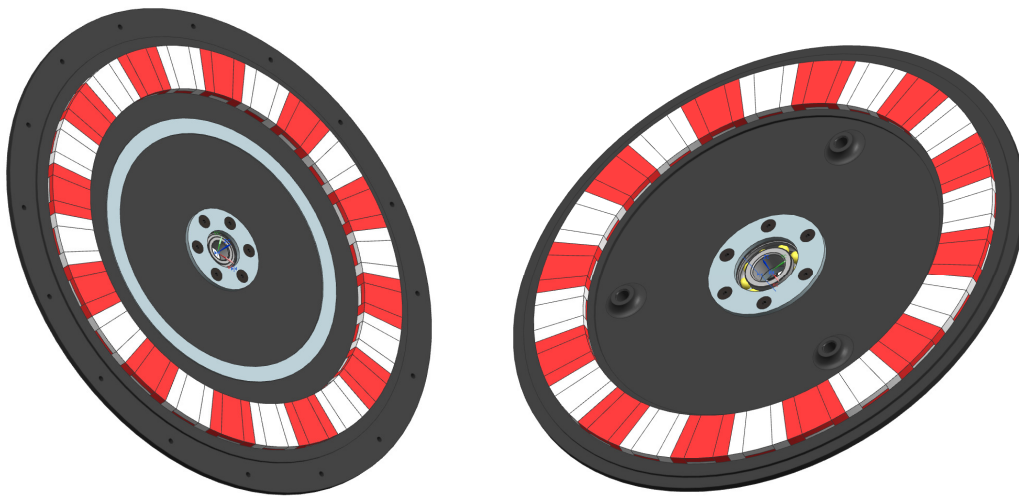


Figure 60: Outer and inner rotor with colorized magnet arrays

The rotors are shown in Figure 60. The outer rotor, on the left, shows a protection ring which would be used if the rotor was to be made from carbon fiber, to protect from the bolts used to separate the motor. The right one, although black, shows how it would be made in aluminum. The three holes are threaded with M10 to allow bolts to be inserted and rotated to force the rotors apart. Because of the strong magnets it is not possible to separate the motor otherwise. If it was made in carbon fiber the three holes for separation would be made by threaded inserts.

The rotor design was analyzed with both aluminum and massive carbon fiber in mind.

S04.1_rotor_inner_alu_sim1 : Solution 1 Result
 Load Case 1, Static Step 1
 Stress - Element-Nodal, Unaveraged, Von-Mises
 Min : 0.17, Max : 378.95, N/mm²(MPa)
 Deformation : Displacement - Nodal Magnitude

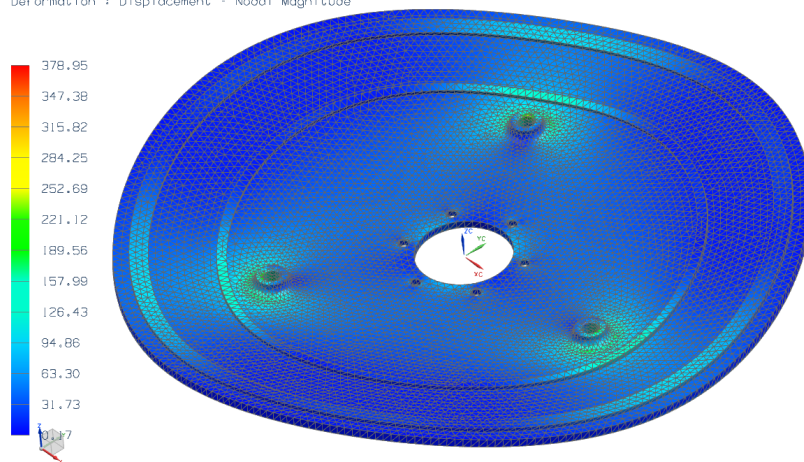


Figure 61: FEM simulation of separation using 3 holes

S04.1_rotor_inner_alu_sim1 : Solution 1 Result
 Load Case 1, Static Step 1
 Stress - Element-Nodal, Unaveraged, Von-Mises
 Min : 0.23, Max : 361.88, N/mm²(MPa)
 Deformation : Displacement - Nodal Magnitude

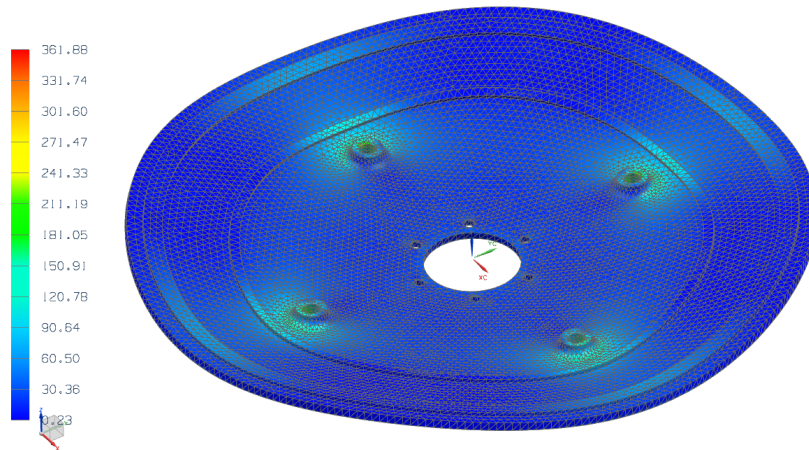


Figure 62: FEM simulation of separation using 4 holes

The simulations of aluminum rotors were used to check if three or four holes should be used for the separation. Since four holes do not significantly reduce the stresses, and the stress concentration of 379 MPa is below alumec's yield strength of 550 MPa there is no reason to use more than three.

The simulation of using DB 420 was difficult, and the results are not conclusive, because the deformations for a 4 mm thick carbon fiber rotor is about 6 cm, even though the stresses are below the tensile strength of 1500 MPa. Any thicker rotor would defeat the purpose of using carbon fiber to save weight.

S04.1_rotor_inner_sheet_sim1 : Separation Result
 Load Case 1, Static Step 1
 Displacement - Nodal, Magnitude
 Min : 0,00, Max : 61,86, mm
 Deformation : Displacement - Nodal Magnitude

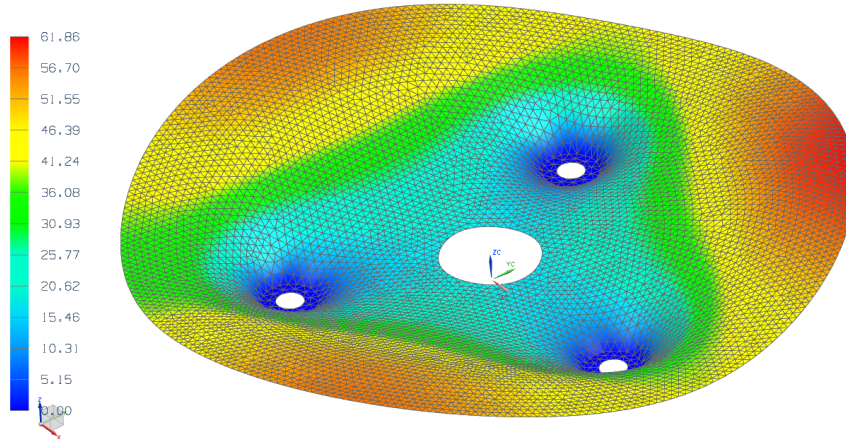


Figure 63: Deformation from separation, 6.2 cm max

S04.1_rotor_inner_sheet_sim1 : Separation Result
 Load Case 1, Static Step 1
 Stress - Element-Nodal, Unaveraged, Von-Mises
 Shell Section : Top
 Min : 0,00, Max : 404,57, N/mm²(MPa)
 Deformation : Displacement - Nodal Magnitude

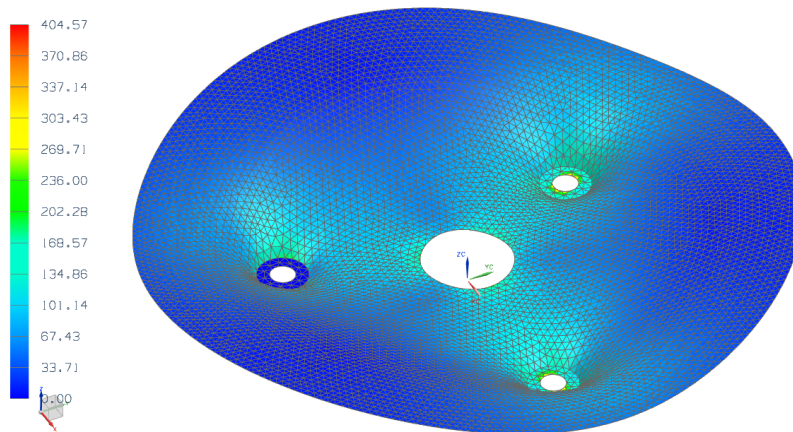


Figure 64: Stresses from separation, 405 MPa max

S04.1_rotor_inner_sheet_sim1 : Separation 3 Result
 Load Case 1, Static Step 1
 Displacement - Nodal, Magnitude
 Min : 0,00, Max : 40,94, mm
 Deformation : Displacement - Nodal Magnitude

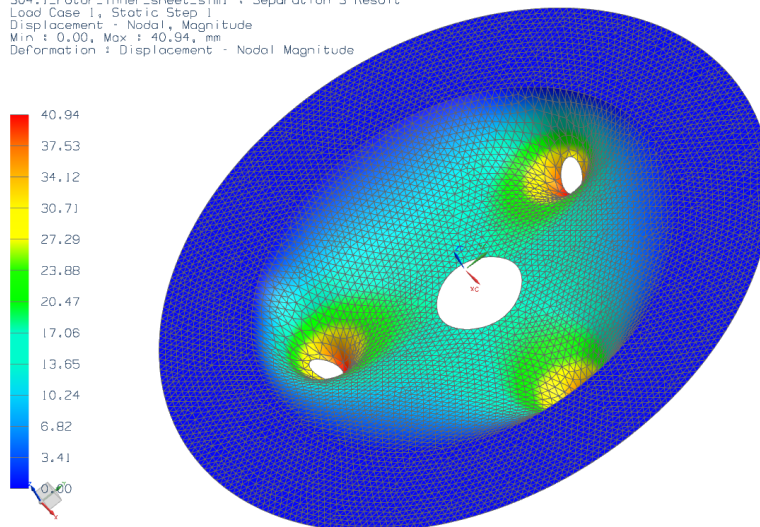


Figure 65: Deformation from separation, 4.1 cm max, using alternative conditions

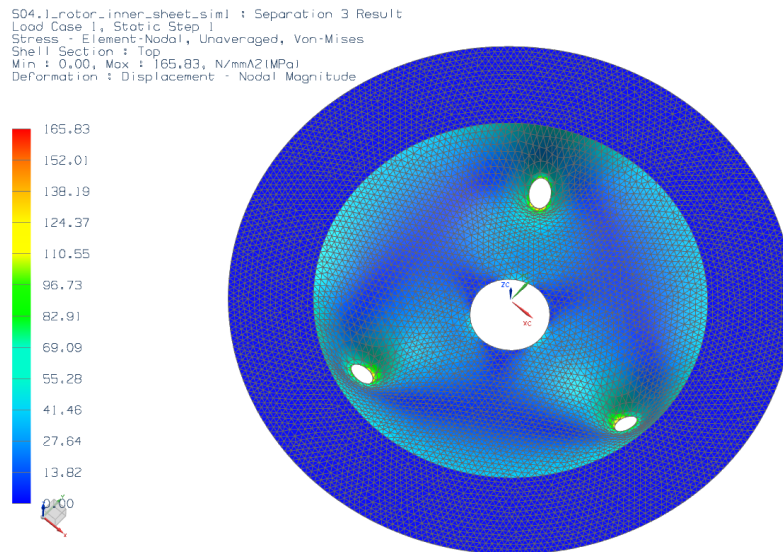


Figure 66: Stresses from separation, 166 MPa max, using alternative conditions

For the rotors we thus have a verified design for using aluminum. We do have a wish for saving even more weight by using massive carbon fiber, but at the time of writing we were still waiting for samples from HPC. The reason is that the material data we have is incomplete, or approximate, and the scenario of the Hallbach array-rotor interface failing or delamination of the rotors is a downright scary one.

3.5. Rim adapters

The rim adapters allow the motor to be mounted into the rim ring in a non-permanent fashion (with regards to the rim adapters). Permanent assemblies are an Achilles' heel if some part should fail or needs adjustment. The new motor design is smaller in diameter than the previous (2011, 2010) and this allows two conical rings to be inserted from each side of the rim, and an array of 16 M4 bolts to keep the motor in place.

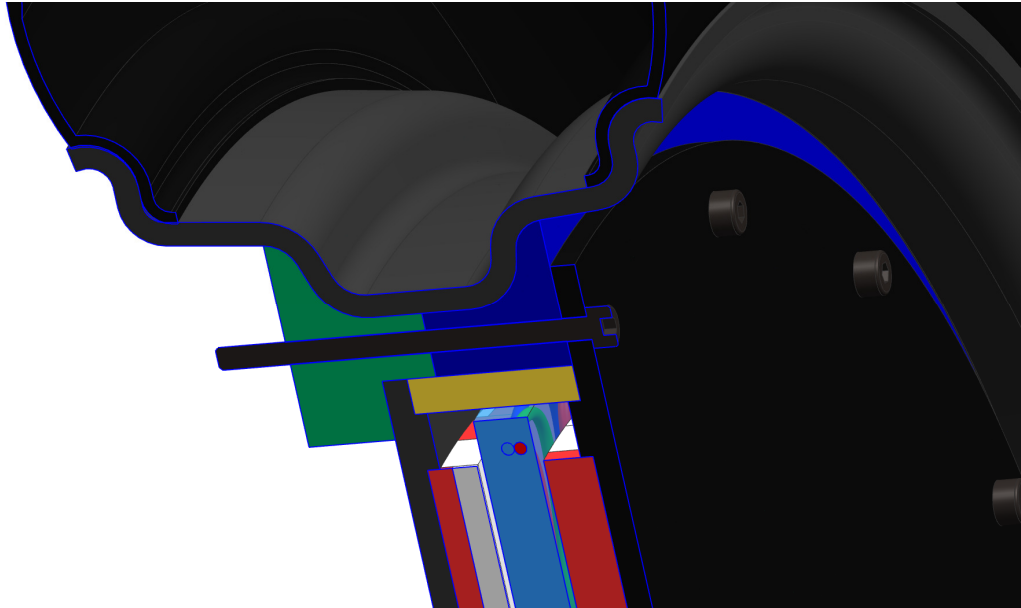


Figure 67: Close up of rim adapters, in green and blue. The yellow section is the rotor spacer

The exact, final size of the rim adapters' surfaces for mating with the rims could not yet be determined, because the exact inner size of the rims remain unknown until they are delivered by HPC. Only then can the outer dimensions be set and the adapter parts released to manufacture.

Since the outer rim adapter will be exposed to sunlight, it must be from a UV-resistant polymer, or else be coated with a UV-blocking paint. During competition the rear wheels will be occluded by aerodynamic covers anyway, but experience from testing shows that the car is tested a lot without wheel covers.

3.6. Test rig and SmartMotor-adapter

Testing the motor thoroughly is imperative, and while SmartMotor's laboratory offers a test bench and virtually unlimited service hours, it must absolutely be possible to mount the motor in the test bench. In my specialization project, I built a test rig from scrap metal and designed a test adapter in aluminum to easily allow for the motor to be tested at SmartMotor's test bench. The concept is proven and can be reused, but the circular shaft hole with a keyway does not fit the new octagonal axle, and the outer bearing housing of the motor is smaller, so new test adapter must be made. The old aluminum plate should not be modified to fit the new motor in case the old motor needs to be tested again.

The SmartMotor test adapter is essential for testing the motor at SmartMotor's test bench. It allows the motor to transfer torque to an opposing motor which can be used to either drive the motor or measure the energy output.

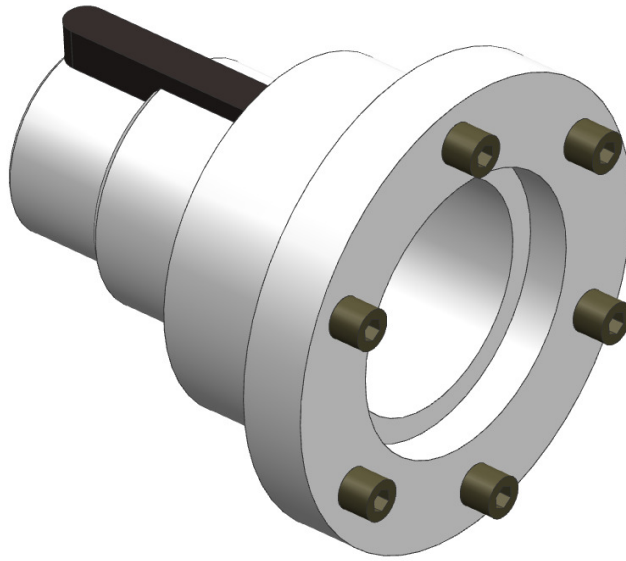


Figure 68: The new test adapter

It is also an incremental improvement of last year's test adapter, with a small end tip that can be inserted into the chuck of an ordinary power drill, so that the drill can be used to rotate the motor wheel. Experience from the 2011 competition revealed that the team needed to drive the motor at cruise RPM to measure the back-induced voltage [reference to last year's report] after a last-minute increase in magnet distance. Since the test adapter was not packed, and it wouldn't fit a drill anyways, that team had to improvise and use a plastic bottle top and bolt to "connect" the power drill to the motor wheel.

4. Conclusions

At this time, many parts are still in production, as we got delayed from staying in the design finalization phase too long and received materials weeks after originally planned. Also some design choices still have to be made.

The design of the front suspension has been very successful, but estimates of the final weight indicate that each front suspension is going to weigh about 2.1 kg, which exceeds the weight goals slightly. The other strengths of the suspension, such as adjustability, spring/damper mechanism, high strength and vibration damping makes this an acceptable sacrifice.

For the motor, we still need to decide between making the rotors in carbon fiber or aluminum. The estimated weight of the motor is 5.7 kg if aluminum is used for the rotors, while it gets reduced to 4.6 kg if we use carbon fiber. This is, in either case, an extremely good improvement over last year's motor wheel which weighed in at a massive 17 kg [2]. The weight reduction will result in better energy efficiency and easier attachment of the motor wheel to the car.

So far, about 80 000 NOK have been spent on the front and rear suspension and steering system combined; and on the motor, about 20 000 NOK. This means that the systems I have been working with are still within budget – more parts will be purchased as the production comes to a finish. And if there are money left over from this year's project execution it will come in handy for the next team. During this project session, 2011-2012, we were working with about 100 000 NOK remaining from the previous team, and did not get financial aid from the sponsor(s) before January.

5. References

1. Gudvangen, H. et al (2011). *Eco-marathon 2012 Project Report*
2. Qviller, A. Stockfleth, T. Bleie, S. Hoel, M. (2011). *Shell Eco-marathon, DNV Fuel Fighter 2011*. Trondheim, Norway: Norwegian University of Science and Technology.
3. Irgens, F. (1999). *Formelsamling mekanikk: statikk, fasthetslære, dynamikk, fluidmekanikk* (3 ed.). Trondheim, Norway: Tapir.
4. Härkegård, G. (2004). *Dimensjonering av maskindeler*. Trondheim, Norway: Tapir Akademiske Forlag
5. Rølvåg, T. (2008). *Design and Optimization of Suspension Systems and Component*. Trondheim, Norway: Department of Machine Design and Materials Technology, Norwegian University of Science and Technology.
6. Vedvik, N. P. (2011). *Composite Materials*. Trondheim, Norway: Norwegian University of Science and Technology.
7. Alcoa (2011). *Fatigue properties*, confidential text on Alumec fatigue properties obtained from Alcoa
8. Various authors (1993). *Proceedings of the Institution of Mechanical Engineers: Vehicle Ride and Handling*. ISBN 0-85298-861
9. Gudem, M. (2006). *Design and evaluation of sports car suspension system*. Trondheim, Norway: Norwegian University of Science and Technology
10. Gillespie, T. D. (1992). *Fundamentals of Vehicle Dynamics*. USA: Society of Automotive Engineers, Inc.
11. SAE (2000). *Bosch Automotive Handbook*. Robert Bosch GmbH.
12. Beckman, B. (2008). *The Physics of Racing*. USA: Burbank.
13. Gudvangen, H. Qviller, A. (2012) *Bolt-carbon fiber tensile tests*.
14. Shell (2011). *Chapter I Official Rules*. Retrieved from http://www.shell.com/home/content/ecomarathon/europe/for_participants/europe_rules/ November 2011
15. Shell (2011). *Ahoy race track map*. Retrieved from http://www.shell.com/home/content/ecomarathon/europe/2012_rotterdam/competition_structure/ November 2011

16. SKF (2012). *Selection of bearing size*. Retrieved from www.skf.com February 2012
17. RenShape solutions, *Casting Resin RenCast*, provided by Lindberg & Lund AS
18. Granta Design Ltd (2011). *CES EduPack 2011*.
19. *Fastener Thread Designations and Definitions Pitch, Minor, Major Diameters*. Retrieved from <http://www.engineersedge.com/hardware/metric-external-thread-sizes1.htm> February 2012

6. Appendices

6.1. Appendix 1: Acknowledgments

I would like to thank the following people for their support, either directly or indirectly, to the progress and success of this project:

- **Knut Einar Aasland**
IPM staff, NTNU
Supervisor
- **Kristina Dalberg**
Det Norske Veritas (DNV)
Main sponsor contact person
- **Bjarne Stolpnessæter**
IPM staff, NTNU
For all the CNC milling of moulds, suspension knuckles and a lot more, for always being open to new machining requests and short delivery times
- **Per Øystein Nortug**
IPM workshop, NTNU
For machining assistance and staying late nights, even weekends, so we could work in the workshop
- **Børge Holen**
IPM workshop, NTNU
For machining assistance
- **Office Administration**
IPM staff, NTNU
For handling all the purchasing orders and payments
- **Arne Gellein**
SINTEF Materialer og Kjemi
For free metal cutting
- **Jan Erik Molde**
Elkraft, NTNU
For machining of motor hub

6.2. Appendix 2: Estimated material data for DB 420 [+45/-45]

Material type: Orthotropic⁷

Table 7: DB 420 physical properties

		Min	Max	Units
Youngs modulus	E1	110	140	GPa
	E2	5	8	GPa
	E3			GPa
Poissons ratio	NU12	0.25	0.30	-
	NU23	0.50	0.60	-
	NU13			-
Shear modulus	G12	3	5	GPa
	G23			GPa
	G13			GPa
Tensile stress	ST1	1500	2000	MPa
	ST2			MPa
	ST3	20	50	MPa
Compressive stress	SC1	800	1200	MPa
	SC2			MPa
	SC3	100	200	MPa
Shear stress	S12	40	80	MPa
	S23			MPa
	S13			MPa
Density		420		g m ²
Density, cured ⁸		1.5		g cm ³
Thickness		0.8		mm
Thickness, cured		0.5		mm

Notes:

*NB: DB420 er en strikket armering bestående av 2 distinkte lag, det er IKKE en vev. Altså gir en ammering en layup [45/-45]
Tykkelse på hvert lag er jo gitt av tettheter og volumfraksjoner, så det finner du greit.
Angående volumfraksjon, vil en rimelig range være 0.50-0.55 med godt vakuum. Slurv og fanteri forøvrig kan gi laver, f.eks. 0.45.*

⁷ The data on this page was acquired from Nils Petter Vedvik by Petter Larsen.

⁸ Empirical data found by measuring DB420 products made by the team

6.3. Appendix 3: Program listings

This appendix includes the manual G-code programming used to machine the front suspension wishbones. These may differ slightly from the programming that was entered into the Fanuc computer on the Makino milling machine in IPM's workshop, e.g. the comments were omitted.

<i>Program: Main</i>	
O0150 ;	Main program for milling front left wishbone
S3000 M03 F1400 G17 G90 ;	
M08 ;	Coolant on
M21 ;	Optional: Mirror X-axis, for right wishbone
M22 ;	Optional: Mirror Y-axis, for right wishbone
M23 ;	Optional: Mirror OFF
G00 X-15. Y0. ;	Move outside material block
Z-90. ;	
G01 Z-103. ;	Prepare cut depth for first cut
M98 P151 L7 ;	Cut seven times with 3mm cuts
G90 ;	Switch back to absolute coordinates just in case
G01 Z-123. ;	Prepare height for final planar cut
M98 P151 L1 ;	Last planar cut
N11 G90 ;	Labeled for graph plot
G01 X-15. ;	
G00 Z-90. ;	
X40. Y-28.8 ;	
G01 Z-106. ;	
X35. ;	
M98 P152 L21 ;	Mill north ear profile
G90 ;	
G00 Z-90. ;	
X40. Y-45.8 ;	
G01 Z-106. ;	
X35. ;	
M98 P152 L21 ;	Mill south ear profile
G90 ;	
G00 Z-90. ;	
X-15. ;	
Y-59.1 ;	
G01 Z-125. ;	
M98 P153 L8 ;	Cut out the bottom angles
G90 ;	
G01 Z-90. ;	Begin safe return to origin
M09 ;	Coolant off
M05 ;	Spindle stop
G00 Z0. ;	To origin
X0. Y0. ;	
M30 ;	Program end/all reset
%	

Program: Rough cut

```
O0151 ;          Program for milling around ears until Z-middle of
he wishbone
; Assumes starting in position X-15. Y0.
G17 G90 ;
G01 X0. ;
Y-41.9 ;
X30. ;
G03 X35. Y-36.9 R5. ;
G01 Y-30.9 ;
G03 X30. Y-25.9 R5. ;
G01 X0. ;
Y-58.9 ;
X30. ;
G03 X35. Y-53.9 R5. ;
G01 Y-47.9 ;
G03 X30. Y-42.9 R5. ;
G01 X0. ;
Y-63.1 ;          To south edge
X61.3 ;          To south-east vertex
Y0. ;          To north-east vertex
X5. ;          To second west edge
Y-20.9 ;          To second north edge of north ear
X40. ;          To second east edge of both ears
Y-58.1 ;          To second south edge
X56.3 ;          To second east edge
Y-5. ;          To second north edge
X10. ;          To third west edge
Y-15.9 ;          To third north edge of north ear
X45. ;
Y-53.1 ;
X50. ;
Y-10. ;
X-15. ;
Y0. ;
G91 ;
G01 Z-3. ;          Lower for next cut
G90 ;
M99 ;
%
```

Program: Ear profile

```
O0152 ; Program for milling ear profiles, operates only in ZX-plane,
caller must modify Y-axis
; Assumes starting in position X35. Z-106. and Y depending on which
is being milled
G18 G90 ; Select ZX-plane for circular interpolation and abs. coords.
G02 X26.5 Z-100. R9.021 ; East radius
G01 X16.2 ;
G02 X8.586 Z-104.739 R8.501 ; West radius
G01 X0. Z-121.910 ; West slope
G91 ;
G01 Y-0.2 ; Strafe for next cut
G90 ;
G01 X8.586 Z-104.739 ; West slope
G03 X16.2 Z-100. R8.501 ; West radius
G01 X26.5 ;
G03 X35. Z-106. R9.021 ; East radius
G91
G01 Y-0.2 ; Strafe for next cut
G90 ;
M99 ;
%
```

Program: Final shape

```
O0153 ; Program for milling angle profile
; Assumes starting in position X-15. Y-59.1
G17 G90 ; Select XY-plane for circular interpolation and abs.
coords.
G01 X0. ;
Y-28. ;
X34.7 Y0. ;
X52. Y-20.6 ;
X42.1 Y-28.9 ;
G03 X43.6 Y-34.2 R3. ;
G01 X61.3 Y-36.7 ;
X57.6 Y63.1 ;
X0. Y-59.1 ;
X-5. ;
G91 ;
G01 Z-2. ; Lower spindle for the next cut
G90 ;
M99 ;
%
```

6.4. Appendix 4: Spreadsheet for simplified vehicle dynamics

Quasi-dynamic vehicle calculations for steering									
Coordinate system									
X	Right/lateral								
Y	Forwards/heading								
Z	Upwards								
All turns left/counter-clockwise, thus the vectors									
All turn radii calculated from differential									
User input in yellow cells :									
Invariants									
Wheel base	1.40 m								
Front track width	1.03 m								
Rear track width	0.80 m								
Car base mass	70.00 kg								
Driver weight	75.00 kg								
Static mass	145.00 kg								
Center of mass X	0.00 m								
Center of mass Y	-1.00 m								
Center of mass Z	0.70 m								
Gravity	9.81 m/s ²								
Case/LCP setup									
Turn radius *	20 m								
Speed	25 km/h								
XY-plane reaction unit vectors									
Frnt left	4.11								
Frnt right	3.90								
Centript frce	2.00								
Frnt left (X,Y)	-0.997429	-0.071665							
Frnt right (X,Y)	-0.997680	-0.068084							
Rear left (X,Y)	-1.000000	0.000000							
Rear right (X,Y)	-1.000000	0.000000							
Per-wheel turn radii and speeds									
Frnt left radius	19.54 m								
Frnt right radius	20.56 m								
Rear left radius	19.49 m								
Rear right radius	20.52 m								
Frnt left speed	6.78 m/s								
Frnt right speed	7.14 m/s								
Rear left speed	6.77 m/s								
Rear right speed	7.12 m/s								
Center of mass turn radii and acceleration									
Cm turn radius	20.00 m	Adjusted for Cm to diff							
Diffrntial arc spd	6.94 m/s	@diff							
Cm arc speed	6.95 m/s	@Cm							
Angular speed	0.35 rad/s	@Cm							
Angular speed	19.90 °/s	@Cm							
Centript accelr	2.41 m/s ²	@Cm							
Centript force	349.67 N	@Cm							
Centript frce (X,Y)	349.46	12.23 @Cm							
Intermediate calculations									
P_w	1,422.45 N	Static weight force							
M_x	-8.56 N m	Moment backwards from centripetal force							
M_y	244.62 N m	Moment laterally from centripetal force							
P_o_z	1,245.92 N	Outer wheels up reaction force							
P_i_z	176.53 N	Inner wheels up reaction force							
Stability	Stable	Unstable => tips over							
P_o_z_clamp	1,245.92 N	Ugly clamping of outer wheels reaction force							
P_i_z_clamp	176.53 N	Ugly clamping of inner wheels reaction force							
Approximate contact patch reaction forces									
WheelForce dir	Lateral	Up/weight							
Frnt left	21.80	90.79 N							
Frnt right	150.21	625.48 N							
Rear left	24.62	102.54 N							
Rear right	153.03	637.23 N							
Check sum	349.67	1,456.03 N							
Ackerman steering angles									
Turn radius ^	m	Frnt left °	Frnt right °	L - R °	L/R %	Cmpl frce °			
30.0	2.72	2.63	0.09	3.5%	1.34				
25.0	3.27	3.14	0.13	4.2%	1.60				
20.0	4.11	3.90	0.21	5.3%	2.00				
15.0	5.52	5.16	0.36	7.1%	2.67				
10.0	8.40	7.58	0.81	10.7%	4.00				
8.0	10.59	9.34	1.26	13.5%	5.00				
6.0	14.32	12.13	2.19	18.1%	6.65				
5.0	17.34	14.24	3.09	21.7%	7.97				
4.0	21.89	17.23	4.66	27.0%	9.93				
3.0	29.40	21.72	7.68	35.4%	13.13				
2.0	43.31	29.10	14.21	48.8%	19.29				

